Tunable porous nanoallotropes prepared from binary nanoparticle superlattices formed at liquid-air interfaces

Thumu Udayabhaskararao,[1] Thomas Altantzis,[2] Lothar Houben,[3,4] Marc Coronado-Puchau,[5]
Judith Langer,[5,6] Ronit Popovitz-Biro,[3] Luis M. Liz-Marzán,[5,6,7] Lela Vuković,[8] Petr Král,[9,10,11]
Sara Bals,[2] Rafal Klajn[1]*

[1]Department of Organic Chemistry, Weizmann Institute of Science, Rehovot 76100, Israel

[2]EMAT, University of Antwerp, Groenenborgerlaan 171, B-2020 Antwerp, Belgium

[3]Department of Chemical Research Support, Weizmann Institute of Science, Rehovot 76100, Israel

[4]Ernst Ruska-Centre for Microscopy and Spectroscopy with Electrons, 52425 Jülich, Germany

[5]CIC biomaGUNE, Paseo de Miramón 182, 20014 Donostia-San Sebastián, Spain

[6]Biomedical Research Networking Center in Bioengineering, Biomaterials, and Nanomedicine (CIBER-BBN), 20014 Donostia-San Sebastián, Spain

[7]Ikerbasque, Basque Foundation for Science, 48013 Bilbao, Spain

[8]Department of Chemistry, University of Texas at El Paso, El Paso, TX 79968, USA

[9]Department of Chemistry, University of Illinois at Chicago, Chicago, IL 60607, USA

[10]Department of Physics, University of Illinois at Chicago, Chicago, IL 60607, USA

[11]Department of Biopharmaceutical Sciences, University of Illinois at Chicago, Chicago, IL 60607, USA

*Correspondence to: rafal.klajn@weizmann.ac.il

Abstract: Self-assembly of inorganic nanoparticles has been used to prepare hundreds of different colloidal crystals, but almost invariably with the restriction that the particles must be densely packed. Here, we show that non-close-packed nanoparticle arrays can be fabricated by selective removal of one of two components comprising binary nanoparticle superlattices. First, a variety of binary nanoparticle superlattices were prepared at the liquid-air interface, including several arrangements that were previously unknown. Molecular dynamics simulations revealed the unique role of the liquid in templating the formation of superlattices not achievable by self-assembly in bulk solution. Second, upon stabilization, all of these binary superlattices could be transformed into distinct "nanoallotropes" – nanoporous materials having the same chemical composition, but differing in their nanoscale architectures.

One Sentence Summary: Binary nanoparticle arrays treated with etchants, selective for one of their components, are transformed into a new family of nanoporous materials.

Main Text: Self-assembly has emerged as the strategy of choice toward generating ordered arrays of nanosized particles. The resulting materials, in particular those assembled from inorganic nanoparticles (NPs) (*1-7*), often exhibit unanticipated optical (*8*), thermoelectric (*9*), magnetic (*10*), catalytic (*11*), and other (*12*) properties. The diversity of structures and presumably the properties of these materials could be greatly enhanced via post-synthetic modifications, which could be used to generate assemblies in which the constituent NPs are ordered yet separated by relatively large distances, that is, non-close-packed (NCP) NP arrays. Although several examples of related materials have been reported, they are limited to highly specific systems, such as those involving highly directional interactions (*13, 14*) or a fine balance between attractive and repulsive forces during self-assembly (*15*). Thus, a general route to NCP NP arrays has been lacking.

One strategy to tackle this limitation could be based on the selective removal (by means of chemical etching) of one type of NPs from binary NP superlattices (BNSLs) (*1*). Depending on the stoichiometry and structure of the initial BNSLs, this method could lead to "nanoallotropes" – materials having the same chemical composition, but differing in their nanoscale architecture. Unfortunately, within BNSLs, the two types of nanoscopic components mutually support each other, and removal of one would inevitably lead to the disruption of the other. Here, we hypothesized that this undesired behavior could be overcome by stabilizing the BNSL by controlled removal of the surfactants from the NP surfaces (*16-18*). If successful, this procedure would serve three purposes: (i) attaching the NPs to the underlying surface, (ii) controlling the coalescence of the NPs, and (iii) activating the sacrificial component of the BNSL toward etching.

We worked with monodisperse batches of Au and Fe_3O_4 NPs [Fig. S1, S2 in the Supplementary Materials (*19*)], which we assembled at the diethylene glycol (DEG)-air interface (step 1 in Fig. 1A), as previously reported (*20*). After transfer onto a carbon-coated transmission electron microscopy (TEM) copper grid (step 2) and a controlled, thermally induced desorption of ligands from the NPs (*17*) (step 3), the samples were exposed to an etchant reacting with only one of the two materials (step 4). As a proof-of-concept, we co-assembled a ~1:1 mixture of 5.2 (±0.4) nm dodecanethiol-protected Au NPs and 10.6 (±0.6) nm oleate-protected Fe_3O_4 NPs into the previously reported (*20*) AB-type binary NP monolayer [Fig. 1B, Fig. S3-S5 (*19*)]. After immobilization onto carbon-coated TEM grids, Fe_3O_4 NPs could be etched out by immersing the substrate into an aqueous solution of HCl, without affecting the order of the gold NPs (Fig. 1C). Figure 1E, for example, shows an ensemble of 250 gold NPs, the positions of which all remained unaffected after HCl etching [see also Figs. S6-S8 (*19*)]. We will refer to the resulting NCP array of Au NPs as vac_1Au_1, where *vac* denotes "vacancy". Alternatively, a square array of self-supporting Fe_3O_4 NPs could be obtained by treating the BNSLs with a cyanide solution, which can selectively dissolve Au NPs (Fig. 1D).

The underlying substrate had a profound effect on the successful fixation of the NPs. The NPs could be readily immobilized on commercial carbon-coated Formvar films as well as on homemade carbon-coated nitrocellulose substrates. However, we found no attachment onto silicon wafers or nitrocellulose lacking a layer of amorphous carbon [Fig. S9 (*19*)]. From these results, we conclude that amorphous carbon facilitated the desorption of organic ligands from the NP surfaces and the formation of a carbonaceous film (*21*), which can serve as an adhesive for the NPs. The carbonaceous films can directly be visualized by TEM [Fig. S10 (*19*)]. Overall, the above procedure allowed for the fabrication of NCP NP superlattices on thin, flexible substrates (see the inset of Fig. 1C), which could subsequently be transferred onto surfaces of choice.

Self-assembly from a ~5:1 mixture of Au and Fe_3O_4 NPs resulted in a different type of BNSL, as shown in Fig. 2A [see also Fig. S11 (*19*)]. This array, featuring alternating clusters of Au NPs and individual Fe_3O_4 NPs, is akin to the previously reported Fe_4C-type BNSL (*22*). However, selective removal of the Fe_3O_4 counterpart allowed us to observe quintets—rather than quartets—of Au NPs arranged in a tetrahedral geometry [Figs. 2B, S12 (*19*)]. To decipher the structure of this and other more complex assemblies (see below), we conducted electron tomography studies (*23, 24*) by acquiring series of 2D projections of the etched arrays over a wide range of tilt angles using high-angle annular dark-field scanning transmission electron microscopy (HAADF-STEM). These studies confirmed that each cluster was composed of five Au NPs [giving rise to stoichiometry vac_1Au_5; see also Figs. S13-S15 (*19*)], and they helped elucidate the mutual packing of the resulting tetrahedra [Fig. 2C, D; see Database S1 for tomography data (*19*)]. The high stability of these tetrahedra could be attributed to partial coalescence of Au NPs, which occurred as a result of ligand desorption (*16-18*). As the structural model in Fig. S16 shows, the vac_1Au_5 array is derived from an incomplete (deficient in Au) AB_6-type BNSL (*19*).

Our method allowed us to control the degree of coalescence by adjusting the time of thermal treatment; extending the heating time from 30 min to 6 hours allowed us to convert an ensemble of tetrahedra into a well-defined array of pseudospherical ~9 nm gold NPs [see also Figs. S17 to S19 (*19*)]. An unexpected effect of heating was that Au NP quintets lacking a strong attachment to the underlying substrate could migrate and be transformed into well-defined sinuous nanowires [(Fig. S20 (*19*)].

Increasing the Au:Fe_3O_4 NP ratio to ~10 led to another type of BNSL, which, after the removal of Fe_3O_4, exhibited features [Figs. 2E, F, and S21-S23 (*19*)] reminiscent of the previously reported (*25*) AB_{13}-type BNSL. The AB_{13}-type BNSL is composed of layers of quartets and quintets of the “B” NPs, following a $(-B_4-B_5-B_4-)_n$ pattern. However, electron tomography studies on our etched material revealed that it consisted of alternating layers of NP quartets and septets (i.e., a $(-B_4-B_7-)_n$ pattern; Fig. 2G, H), corresponding to an AB_{11} stoichiometry of the precursor BNSL [see also the discussion in Fig. S24 (*19*)]. Similar to the AB_6-type BNSLs, the AB_{11} arrays could be thermally transformed by partial sintering of the constituent Au NPs, resulting in nanoporous membranes [Fig. S25, bottom (*19*)].

However, when the ratio of Au to Fe_3O_4 NPs was decreased to ~4 and a more polydisperse batch of Au NPs (4.9 ± 0.7 nm) was used, we observed the formation of BNSLs, within which the Au NPs were arranged into zigzag-like patterns [Fig. S26 (*19*)]. Electron tomography analysis showed that this BNSL consisted of stacked NP layers having an AB_4 stoichiometry [Fig. 2I, J; Figs. S27 and S28 (*19*)], where “A” denotes a Fe_3O_4 NP and “B” – large, medium, and small Au NPs in a 1:2:1 ratio (for example, the NCP array shown in Fig. 2I consists of 6.2 nm, 5.3 nm, and 4.1 nm Au NPs). The fact that highly crystalline arrays could be assembled even from relatively polydisperse batches of NPs highlights the tendency of NPs to maximize the packing at the DEG-air interface. In fact, analysis of the AB_4, AB_6, and AB_{11} BNSLs showed that they all share the same densely packed initial (bottom) monolayer [see Fig. 2D, H, J and the structural models in Figs. S16, S25, and S29 (*19*)].

The formation of the above AB_4, AB_6, AB_{11}, and other (see below) structures not observed during self-assembly in 3D (i.e., bulk solution) suggests a profound effect of DEG on the assembly process (*26, 27*). To disclose the mechanisms governing self-assembly in our system, we performed precise atomistic molecular dynamics (MD) simulations of NPs at different liquid-air interfaces. These simulations, detailed in the Supplementary Materials, revealed that the role of DEG in guiding NP self-assembly is the result of a combination of several effects (*19*). First, the coupling energies of both types of NPs to DEG are large compared with the NP-NP coupling energies between exposed or partly submerged NPs [Tables S1, S2 (*19*)]. Hence, the NPs exhibit a high affinity to the surface of the underlying liquid, which they tend to cover in the most efficient way. Analysis of BNLSs assembled on the surface of DEG showed that as much as >50% of the lattice energies originates from NP-DEG, rather than NP-NP coupling (*19*). Second, both dodecanethiol-protected Au NPs and oleate-protected Fe_3O_4 NPs preferentially submerge in DEG to about half their diameter (Fig. 2K, L). As a result, DEG can organize the bottom layer of NPs in a way that may not be achievable during self-assembly in bulk solution. Finally, the coupling energy of the NPs to DEG per unit surface area of NP is approximately the same for both types of NPs. Thus, both Au and Fe_3O_4 NPs have a similar affinity towards the surface of DEG, from which they can displace each other during the self-assembly process. Taken together, these effects show that DEG can modify the free energies of BNSLs, favoring the formation of otherwise unstable BNSLs.

When the same polydisperse (4.9 ± 0.7 nm) Au and monodisperse 10.6 nm Fe_3O_4 NPs were used in a ~5:1 ratio, we observed the formation of an unprecedented quasi-ternary BNSL with a stoichiometry ABC_4, where "B" denotes a small (~4.0 nm) and "C" – a large (~5.5 nm) Au NP [Fig. S30 (*19*)]. Subjecting this superlattice to our stabilization–etching procedure afforded an NCP $vac_1Au_1Au'_4$ array shown in Fig. 2M-P (here, Au and Au′ denote small and large Au NPs, respectively) [see also Figs. S31-S34 (*19*)]. Within the ABC_4-type BNSL, the bottom-most Au and Fe_3O_4 NPs have their bottom boundaries (rather than the equatorial cross-sections) at the same level. However, the "half-submergence condition" is still satisfied for both NP types if one considers the two 5.5 nm Au NPs placed on top of each other (labeled C and C′ in Fig. 2P) as a single, elongated NP. Electron tomography studies could not resolve individual NPs within these putative dimers, suggesting that they undergo a partial coalescence (see cyan and red in Fig. 2O).

Importantly, our methodology could be extended to multilayers [Figs. S35-S44 (*19*)], which is exemplified for a novel AB_4-type BNSL [Fig. 3A, S40 (*19*)]. This BNSL was obtained by co-assembly of 5.2 nm Au and 10.6 nm Fe_3O_4 NPs premixed in a ~4:1 ratio, where the thickness of the superlattice depended on the amount of NPs applied at the liquid-air interface. For example, HAADF-STEM tomography revealed that the NCP superlattice shown in Fig. 3B obtained by etching the corresponding BNSL (Fig. 3A) was a hexalayer [cf. Figs. 3C, S43; see also Database S1 (*19*)]. Upon extended (>1 hr) heating at 70°C, the original AB_4-type array was transformed into the exotic pattern shown in Fig. 3D [see also Fig. S42 (*19*)], whose structure remains to be identified. Detailed theoretical analysis in the Supplementary Materials confirms that our technique can in principle be extended to NCP arrays having thicknesses approaching macroscopic dimensions (*19*).

Our methodology can also be applied to NP building blocks of other sizes. For example, in Fig. 3F, G, we extended the average distance between 5.2 nm Au NPs within *vac*$_1$Au$_1$ arrays from 12.5 to 15.3 nm by simply increasing the size of the Fe_3O_4 NPs with which they were co-assembled from 10.6 to 13.0 nm. These results indicate the ability to pattern solid substrates comprising nanoscopic Au domains, with subnanometer precision. When the sizes of both Au (5.2 nm) and Fe_3O_4 (10.6 nm) NPs were decreased (to 3.0 and 8.4 nm, respectively), many of the BNSLs and the resulting NCP arrays could be recreated on a smaller scale [see Fig. S45 (*19*)]. Similarly, working with mixtures of 5.2 nm Au NPs and 8.4 nm Fe_3O_4, we obtained AB-, AB_4-, ABC_4-type, and other BNSLs described above [Fig. S46 (*19*)]. In addition, the modified NP size ratio resulted in novel NP arrays, such as the *vac*$_1$Au$_2$-type and the *vac*$_4$Au$_2$-type structures shown in Fig. 3H, I [see also Fig. S47 (*19*)]. The main drawbacks of our method lie in the inherent difficulties in preparing defect-free BNSLs, which limited the size of single-crystalline domains of BNSLs, and hence of NCP arrays, up to several micrometers. In addition, it has proven challenging to control the film thickness throughout the entire area of the sample—for example, a 1:1 mixture of Au and Fe_3O_4 NPs predicted to give rise to a monolayer of the AB-type BNSL afforded a ~20:1:1 mixture of monolayer, bilayer, and non-coated substrate.

We envision that NCP NP arrays will have a wide range of interesting optical, mechanical, catalytic, and other properties. As an example, we examined several different NP arrays as substrates for surface-enhanced Raman scattering (SERS) and found that the *vac*$_1$Au$_{11}$-type array has superior signal enhancement properties, as compared to *vac*$_1$Au$_5$ (Fig. 4) This is in agreement with a significantly higher density of electromagnetic hotspots at nm-sized gaps between NPs within the multilayer structure, into which analyte molecules can readily diffuse through the NCP crystalline lattice (*19*). An attractive avenue will be to utilize the well-defined nanopores within these materials for trapping active protein molecules. An important aspect of our procedure is that it leads to surfactant-free gold surfaces, amenable to facile functionalization with thiolated ligands. Our results on multilayers suggest that this method could be readily extended to three-dimensional assemblies, including binary superlattices comprising nonspherical NPs (*28*), quasicrystalline arrays (*29*), and ternary superlattices (*30*).

References and Notes:

1. E. V. Shevchenko, D. V. Talapin, N. A. Kotov, S. O'Brien, C. B. Murray, Structural diversity in binary nanoparticle superlattices, *Nature* **439**, 55-59 (2006).
2. N. A. Kotov, F. C. Meldrum, C. Wu, J. H. Fendler, Monoparticulate Layer and Langmuir-Blodgett-Type Multiparticulate Layers of Size-Quantized Cadium-Sulfide Clusters - A Colloid-Chemical Approach to Superlattice Construction, *J. Phys. Chem.* **98**, 2735-2738 (1994).
3. S. Y. Park, A. K. R. Lytton-Jean, B. Lee, S. Weigand, G. C. Schatz, C. A. Mirkin, DNA-programmable nanoparticle crystallization, *Nature* **451**, 553-556 (2008).

4. Z. Y. Tang, Z. L. Zhang, Y. Wang, S. C. Glotzer, N. A. Kotov, Self-assembly of CdTe nanocrystals into free-floating sheets, *Science* **314**, 274-278 (2006).
5. D. Nykypanchuk, M. M. Maye, D. van der Lelie, O. Gang, DNA-guided crystallization of colloidal nanoparticles, *Nature* **451**, 549-552 (2008).
6. G. Singh, H. Chan, A. Baskin, E. Gelman, N. Repnin, P. Král, R. Klajn, Self-assembly of magnetite nanocubes into helical superstructures, *Science* **345**, 1149-1153 (2014).
7. T. Wang, J. Q. Zhuang, J. Lynch, O. Chen, Z. L. Wang, X. R. Wang, D. LaMontagne, H. M. Wu, Z. W. Wang, Y. C. Cao, Self-Assembled Colloidal Superparticles from Nanorods, *Science* **338**, 358-363 (2012).
8. E. V. Shevchenko, M. Ringler, A. Schwemer, D. V. Talapin, T. A. Klar, A. L. Rogach, J. Feldmann, A. P. Alivisatos, Self-assembled binary superlattices of CdSe and Au nanocrystals and their fluorescence properties, *J. Am. Chem. Soc.* **130**, 3274-3275 (2008).
9. M. Ibanez, Z. S. Luo, A. Genc, L. Piveteau, S. Ortega, D. Cadavid, O. Dobrozhan, Y. Liu, M. Nachtegaal, M. Zebarjadi, J. Arbiol, M. V. Kovalenko, A. Cabot, High-performance thermoelectric nanocomposites from nanocrystal building blocks, *Nat. Commun.* **7**, 10766 (2016).
10. A. G. Dong, J. Chen, X. C. Ye, J. M. Kikkawa, C. B. Murray, Enhanced Thermal Stability and Magnetic Properties in NaCl-Type FePt-MnO Binary Nanocrystal Superlattices, *J. Am. Chem. Soc.* **133**, 13296-13299 (2011).
11. Y. J. Kang, X. C. Ye, J. Chen, Y. Cai, R. E. Diaz, R. R. Adzic, E. A. Stach, C. B. Murray, Design of Pt-Pd Binary Superlattices Exploiting Shape Effects and Synergistic Effects for Oxygen Reduction Reactions, *J. Am. Chem. Soc.* **135**, 42-45 (2013).
12. J. J. Urban, D. V. Talapin, E. V. Shevchenko, C. R. Kagan, C. B. Murray, Synergism in binary nanocrystal superlattices leads to enhanced p-type conductivity in self-assembled PbTe/Ag_2Te thin films, *Nat. Mater.* **6**, 115-121 (2007).
13. M. P. Boneschanscher, W. H. Evers, J. J. Geuchies, T. Altantzis, B. Goris, F. T. Rabouw, S. A. P. van Rossum, H. S. J. van der Zant, L. D. A. Siebbeles, G. Van Tendeloo, I. Swart, J. Hilhorst, A. V. Petukhov, S. Bals, D. Vanmaekelbergh, Long-range orientation and atomic attachment of nanocrystals in 2D honeycomb superlattices, *Science* **344**, 1377-1380 (2014).
14. H. X. Lin, S. M. Lee, L. Sun, M. Spellings, M. Engel, S. C. Glotzer, C. A. Mirkin, Clathrate colloidal crystals, *Science* **355**, 931-935 (2017).
15. A. M. Kalsin, M. Fialkowski, M. Paszewski, S. K. Smoukov, K. J. M. Bishop, B. A. Grzybowski, Electrostatic self-assembly of binary nanoparticle crystals with a diamond-like lattice, *Science* **312**, 420-424 (2006).
16. C. J. Kiely, J. Fink, M. Brust, D. Bethell, D. J. Schiffrin, Spontaneous ordering of bimodal ensembles of nanoscopic gold clusters, *Nature* **396**, 444-446 (1998).
17. Y. X. Yu, C. A. Bosoy, D. M. Smilgies, B. A. Korgel, Self-Assembly and Thermal Stability of Binary Superlattices of Gold and Silicon Nanocrystals, *J. Phys. Chem. Lett.* **4**, 3677-3682 (2013).
18. T. Altantzis, Z. J. Yang, S. Bals, G. Van Tendeloo, M. P. Pileni, Thermal Stability of $CoAu_{13}$ Binary Nanoparticle Superlattices under the Electron Beam, *Chem. Mater.* **28**, 716-719 (2016).

19. Materials and methods are available as supplementary materials on *Science* Online.
20. A. G. Dong, J. Chen, P. M. Vora, J. M. Kikkawa, C. B. Murray, Binary nanocrystal superlattice membranes self-assembled at the liquid-air interface, *Nature* **466**, 474-477 (2010).
21. Y. C. Jiao, D. D. Han, Y. Ding, X. F. Zhang, G. N. Guo, J. H. Hu, D. Yang, A. G. Dong, Fabrication of three-dimensionally interconnected nanoparticle superlattices and their lithium-ion storage properties, *Nat. Commun.* **6**, 6420 (2015).
22. E. V. Shevchenko, D. V. Talapin, C. B. Murray, S. O'Brien, Structural characterization of self-assembled multifunctional binary nanoparticle superlattices, *J. Am. Chem. Soc.* **128**, 3620-3637 (2006).
23. H. Friedrich, C. J. Gommes, K. Overgaag, J. D. Meeldijk, W. H. Evers, B. de Nijs, M. P. Boneschanscher, P. E. de Jongh, A. J. Verkleij, K. P. de Jong, A. van Blaaderen, D. Vanmaekelbergh, Quantitative Structural Analysis of Binary Nanocrystal Superlattices by Electron Tomography, *Nano Lett.* **9**, 2719-2724 (2009).
24. M. P. Boneschanscher, W. H. Evers, W. K. Qi, J. D. Meeldijk, M. Dijkstra, D. Vanmaekelbergh, Electron Tomography Resolves a Novel Crystal Structure in a Binary Nanocrystal Superlattice, *Nano Lett.* **13**, 1312-1316 (2013).
25. E. V. Shevchenko, D. V. Talapin, S. O'Brien, C. B. Murray, Polymorphism in AB_{13} nanoparticle superlattices: An example of semiconductor-metal metamaterials, *J. Am. Chem. Soc.* **127**, 8741-8747 (2005).
26. V. Aleksandrovic, D. Greshnykh, I. Randjelovic, A. Fromsdorf, A. Kornowski, S. V. Roth, C. Klinke, H. Weller, Preparation and electrical properties of cobalt-platinum nanoparticle monolayers deposited by the Langmuir-Blodgett technique, *ACS Nano* **2**, 1123-1130 (2008).
27. A. G. Dong, X. C. Ye, J. Chen, C. B. Murray, Two-Dimensional Binary and Ternary Nanocrystal Superlattices: The Case of Monolayers and Bilayers, *Nano Lett.* **11**, 1804-1809 (2011).
28. X. C. Ye, J. Chen, M. Engel, J. A. Millan, W. B. Li, L. Qi, G. Z. Xing, J. E. Collins, C. R. Kagan, J. Li, S. C. Glotzer, C. B. Murray, Competition of shape and interaction patchiness for self-assembling nanoplates, *Nat. Chem.* **5**, 466-473 (2013).
29. Z. J. Yang, J. J. Wei, P. Bonville, M. P. Pileni, Beyond Entropy: Magnetic Forces Induce Formation of Quasicrystalline Structure in Binary Nanocrystal Superlattices, *J. Am. Chem. Soc.* **137**, 4487-4493 (2015).
30. W. H. Evers, H. Friedrich, L. Filion, M. Dijkstra, D. Vanmaekelbergh, Observation of a Ternary Nanocrystal Superlattice and Its Structural Characterization by Electron Tomography, *Angew. Chem. Int. Ed.* **48**, 9655-9657 (2009).
31. T. L. Wen, S. A. Majetich, Ultra-Large-Area Self-Assembled Monolayers of Nanoparticles, *ACS Nano* **5**, 8868-8876 (2011).
32. S. Stoeva, K. J. Klabunde, C. M. Sorensen, I. Dragieva, Gram-scale synthesis of monodisperse gold colloids by the solvated metal atom dispersion method and digestive ripening and their organization into two- and three-dimensional structures, *J. Am. Chem. Soc.* **124**, 2305-2311 (2002).

33. B. H. Wu, H. Y. Yang, H. Q. Huang, G. X. Chen, N. F. Zheng, Solvent effect on the synthesis of monodisperse amine-capped Au nanoparticles, *Chinese Chem. Lett.* **24**, 457-462 (2013).
34. T. Zdobinsky, P. S. Maiti, R. Klajn, Support Curvature and Conformational Freedom Control Chemical Reactivity of Immobilized Species, *J. Am. Chem. Soc.* **136**, 2711-2714 (2014).
35. J. Park, K. J. An, Y. S. Hwang, J. G. Park, H. J. Noh, J. Y. Kim, J. H. Park, N. M. Hwang, T. Hyeon, Ultra-large-scale syntheses of monodisperse nanocrystals, *Nat. Mater.* **3**, 891-895 (2004).
36. A. E. Saunders, B. A. Korgel, Observation of an AB phase in bidisperse nanocrystal superlattices, *ChemPhysChem* **6**, 61-65 (2005).
37. E. V. Shevchenko, D. V. Talapin, A. L. Rogach, A. Kornowski, M. Haase, H. Weller, Colloidal synthesis and self-assembly of $CoPt_3$ nanocrystals, *J. Am. Chem. Soc.* **124**, 11480-11485 (2002).
38. B. W. Goodfellow, M. R. Rasch, C. M. Hessel, R. N. Patel, D. M. Smilgies, B. A. Korgel, Ordered Structure Rearrangements in Heated Gold Nanocrystal Superlattices, *Nano Lett.* **13**, 5710-5714 (2013).
39. W. van Aarle, W. J. Palenstijn, J. De Beenhouwer, T. Altantzis, S. Bals, K. J. Batenburg, J. Sijbers, The ASTRA Toolbox: A platform for advanced algorithm development in electron tomography, *Ultramicroscopy* **157**, 35-47 (2015).
40. J. B. He, X. M. Lin, H. Chan, L. Vuković, P. Král, H. M. Jaeger, Diffusion and Filtration Properties of Self-Assembled Gold Nanocrystal Membranes, *Nano Lett.* **11**, 2430-2435 (2011).
41. M. K. Bera, H. Chan, D. F. Moyano, H. Yu, S. Tatur, D. Amoanu, W. Bu, V. M. Rotello, M. Meron, P. Král, B. H. Lin, M. L. Schlossman, Interfacial Localization and Voltage-Tunable Arrays of Charged Nanoparticles, *Nano Lett.* **14**, 6816-6822 (2014).
42. H. Zhao, S. Sen, T. Udayabhaskararao, M. Sawczyk, K. Kučanda, D. Manna, P. K. Kundu, J.-W. Lee, P. Král, R. Klajn, Reversible trapping and reaction acceleration within dynamically self-assembling nanoflasks, *Nat. Nanotech.* **11**, 82-88 (2016).
43. J. C. Phillips, R. Braun, W. Wang, J. Gumbart, E. Tajkhorshid, E. Villa, C. Chipot, R. D. Skeel, L. Kale, K. Schulten, Scalable molecular dynamics with NAMD, *J. Comput. Chem.* **26**, 1781-1802 (2005).
44. K. Vanommeslaeghe, E. Hatcher, C. Acharya, S. Kundu, S. Zhong, J. Shim, E. Darian, O. Guvench, P. Lopes, I. Vorobyov, A. D. MacKerell, CHARMM General Force Field: A Force Field for Drug-Like Molecules Compatible with the CHARMM All-Atom Additive Biological Force Fields, *J. Comput. Chem.* **31**, 671-690 (2010).
45. W. B. Yu, X. B. He, K. Vanommeslaeghe, A. D. MacKerell, Extension of the CHARMM general force field to sulfonyl-containing compounds and its utility in biomolecular simulations, *J. Comput. Chem.* **33**, 2451-2468 (2012).
46. K. Vanommeslaeghe, A. D. MacKerell, Automation of the CHARMM General Force Field (CGenFF) I: Bond Perception and Atom Typing, *J. Chem. Inf. Model.* **52**, 3144-3154 (2012).

47. K. Vanommeslaeghe, E. P. Raman, A. D. MacKerell, Automation of the CHARMM General Force Field (CGenFF) II: Assignment of Bonded Parameters and Partial Atomic Charges, *J. Chem. Inf. Model.* **52**, 3155-3168 (2012).
48. T. Darden, D. York, L. Pedersen, Particle mesh Ewald: An N·log(N) method for Ewald sums in large systems, *J. Chem. Phys.* **98**, 10089-10092 (1993).
49. W. Humphrey, A. Dalke, K. Schulten, VMD: Visual molecular dynamics, *J. Mol. Graph. Model.* **14**, 33-38 (1996).
50. L. Vuković, A. Madriaga, A. Kuzmis, A. Banerjee, A. Tang, K. Tao, N. Shah, P. Král, H. Onyuksel, Solubilization of Therapeutic Agents in Micellar Nanomedicines, *Langmuir* **29**, 15747-15754 (2013).
51. A. Grossfield, WHAM: the weighted histogram analysis method; University of Rochester Medical Center: Rochester, NY, 2012, accessed April 2017.
52. S. Kumar, D. Bouzida, R. H. Swendsen, P. A. Kollman, J. M. Rosenberg, The weighted histogram analysis method for free-energy calculations on biomolecules. 1. The method, *J. Comput. Chem.* **13**, 1011-1021 (1992).

Acknowledgments: This work was supported by the European Research Council (grants 336080 CONFINEDCHEM to R.K. and 335078 COLOURATOM to S.B.), the Rothschild Caesarea Foundation (R.K.), the NSF (Division of Materials Research, grant 1506886) (P.K.), the European Commission (grant EUSMI 731019 to L.M.L.-M. and S.B.), and the startup funding from the University of Texas at El Paso (L.V.). L.M.L.-M. acknowledges funding from the Spanish Ministerio de Economía y Competitividad (grant MAT2013-46101-R). T.A. acknowledges funding from the Research Foundation Flanders (FWO, Belgium) through a postdoctoral grant. The computer support was provided by the Texas Advanced Computing Center. All data are reported in the main text and supplementary materials.

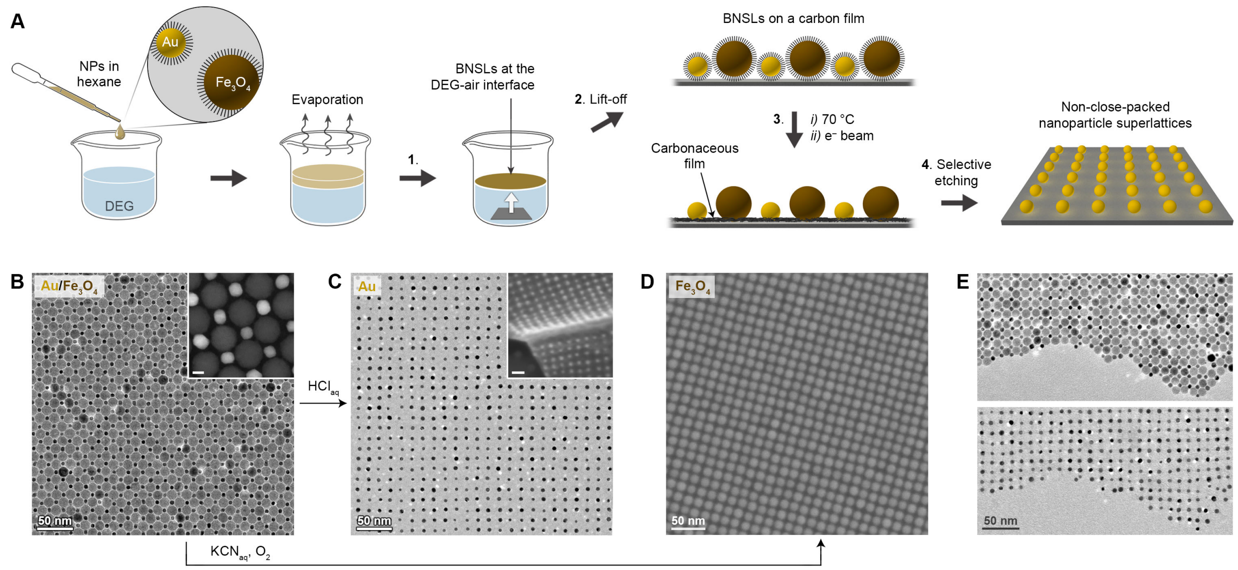

Fig. 1. Preparation of non-close-packed nanoparticle arrays. (**A**) Schematic illustration of the method ("e$^-$ beam" denotes a ~10 min exposure to the electron beam of a transmission electron microscope (TEM); NPs = nanoparticles; BNSL = binary nanoparticle superlattice). (**B**) TEM image of an AB-type BNSL. The image in the inset was recorded in HAADF-STEM mode. (**C**) TEM image of an NCP array of Au NPs (vac_1Au_1) obtained by selective removal of Fe_3O_4. Inset: scanning electron microscopy (SEM) image showing the flexible nature of the underlying film. (**D**) SEM image of an NCP array of Fe_3O_4 NPs obtained by selective removal of Au [note that under the temperature of 70 °C is not sufficient to remove the protective coating from the Fe_3O_4 NPs (*21*); the array remains stable because the relatively large Fe_3O_4 NPs mutually support one another]. Scale bars in the insets correspond to 5 nm (center) and 20 nm (left). (**E**) An edge of an AB-type BNSL before (top) and after (bottom) Fe_3O_4 etching.

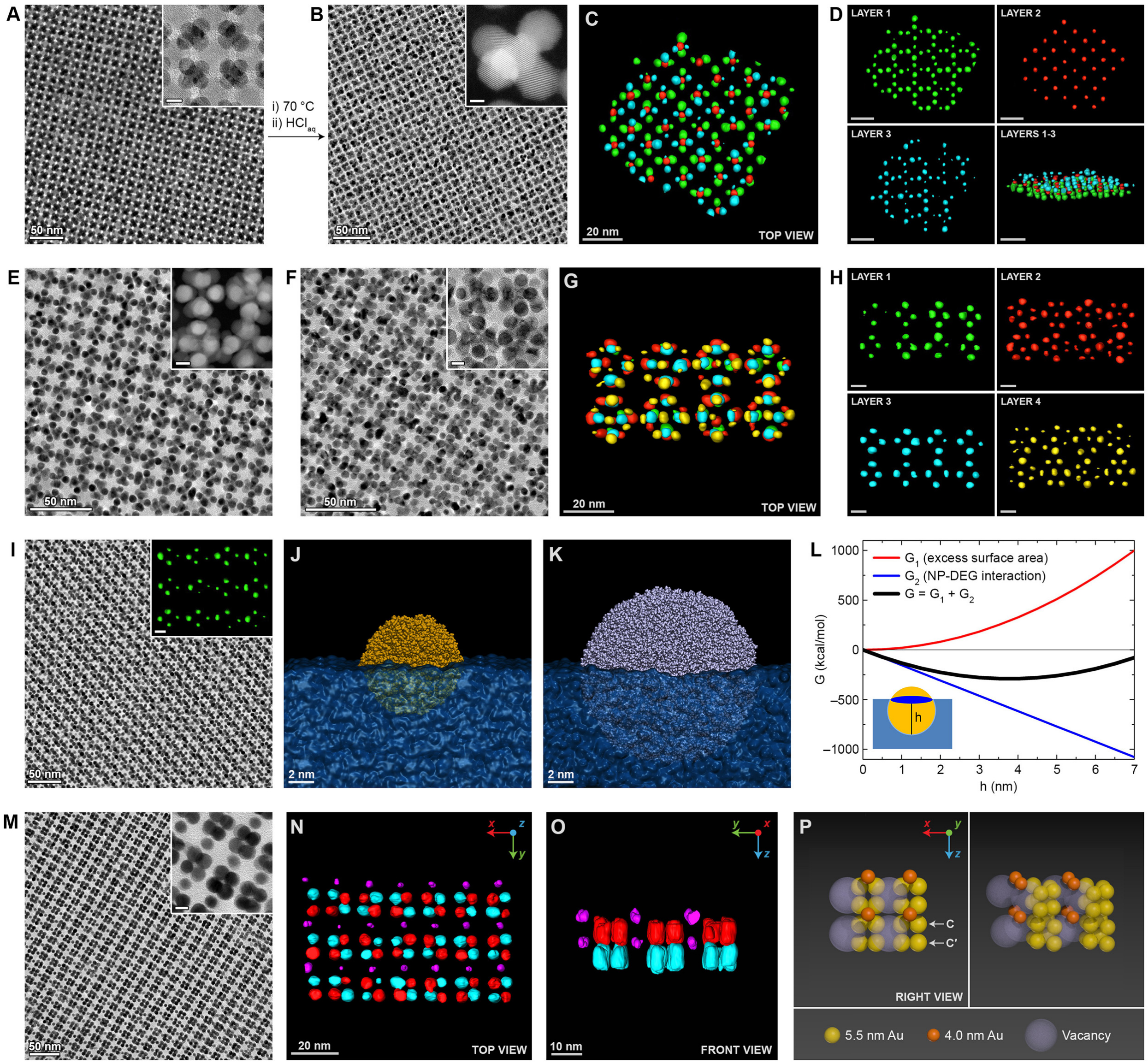

Fig. 2. Structural diversity and characterization of NCP NP arrays. (**A**) TEM image of an AB_6-type BNSL (here, lacking the top layer of Au NPs). (**B**) TEM image of a *vac*$_1$Au$_5$-type array. (**C**) 3D representation of a part of the reconstructed segmented volume of a *vac*$_1$Au$_5$-type array. The different colors correspond to different layers of NPs along the *z*-axis. (**D**) Different layers of the *vac*$_1$Au$_5$ array shown separately for clarity. In the bottom right image, the structure is tilted by 80° to 85° around the *x*-axis. The scale bars correspond to 20 nm. (**E, F**) TEM images of *vac*$_1$Au$_{11}$-type arrays terminated with two different layers of Au NPs. (**G**) 3D representation of a part of the reconstructed segmented volume of a *vac*$_1$Au$_{11}$-type array at different viewing directions. (**H**) Four different layers of a *vac*$_1$Au$_{11}$-type array shown separately for clarity. Scale bars = 10 nm. (**I**) TEM image of a *vac*$_1$Au$_1$Au$_2$′Au″$_1$-type array (Au, Au′, and Au″ denote differently sized Au NPs) Inset: bottom layer of *vac*$_1$Au$_1$Au$_2$′Au″$_1$-type array resolved by electron tomography (scale bar = 10 nm). (**J, K**) Atomistic models of a dodecanethiol-functionalized 5 nm Au NP (J) and an oleate-functionalized 10 nm Fe_3O_4 NP (K) relaxed at the DEG-vacuum interface. (**L**) Free

energy as a function of immersion height, h, for a 5 nm Au NP (protected with a 1 nm-thick ligand shell) immersed into DEG. Red: energy cost to create excess DEG surface area; blue: favorable binding free energy of DEG and Au NP; black: total energy. (**M**) TEM image of a $vac_1\text{Au}_1\text{Au}'_4$-type array. (**N**, **O**) 3D representation of a part of the reconstructed segmented volume of a $vac_1\text{Au}_1\text{Au}'_4$-type array at different viewing directions. In (O), entities colored in red and cyan correspond to two Au NPs on top of each other. (**P**) Structural model of the $vac_1\text{Au}_1\text{Au}'_4$-type array. The images in the insets in B, E, and I have been recorded in an HAADF-STEM mode. Scale bars in the insets correspond to 5 nm unless indicated otherwise.

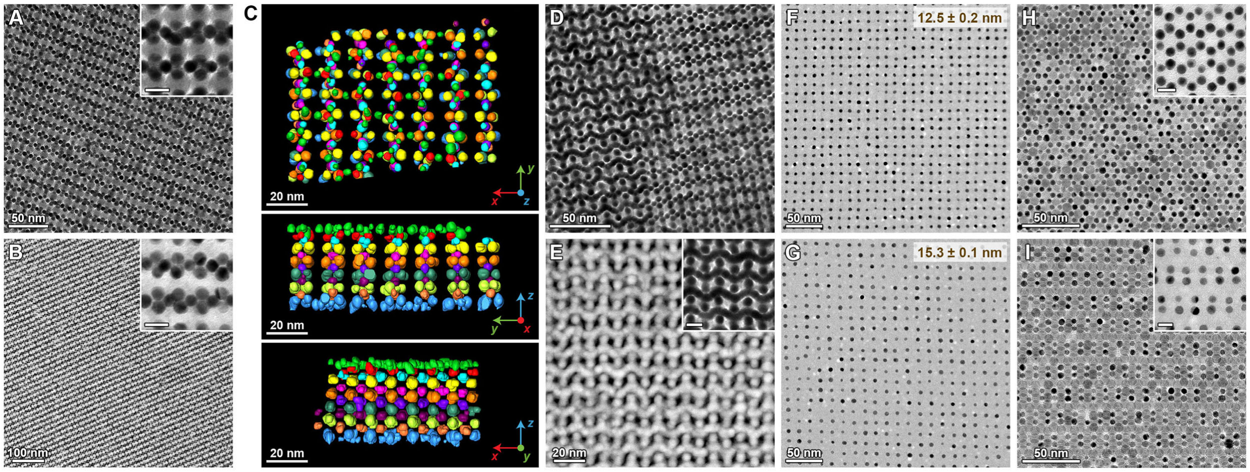

Fig. 3. Extension to multilayers and other nanoparticle sizes. (**A**) TEM image of an AB_4-type binary superlattice. (**B**) TEM image of a $vac_1\text{Au}_4$-type array. (**C**) 3D representation of a part of the reconstructed segmented volume of a hexalayer of a $vac_1\text{Au}_4$-type array at different viewing directions. (**D**) TEM image showing the coexistence of two different types of AB_4 BNSLs and the epitaxial relationship between them. (**E**) HAADF-STEM image of a $vac_1\text{Au}_4$-type array. (**F**, **G**) TEM images of $vac_1\text{Au}_1$-type arrays obtained from BNSLs co-assembled from 5.2 nm Au NPs with (F) 10.6 nm and (G) 13.0 nm Fe_3O_4. (**H**) TEM image of an AB_2-type BNSL and the corresponding (post-etching) $vac_1\text{Au}_2$-type array (inset). (**I**) TEM image of an A_2B-type BNSL and the corresponding $vac_2\text{Au}$-type array (inset). Scale bars in the insets correspond to 10 nm.

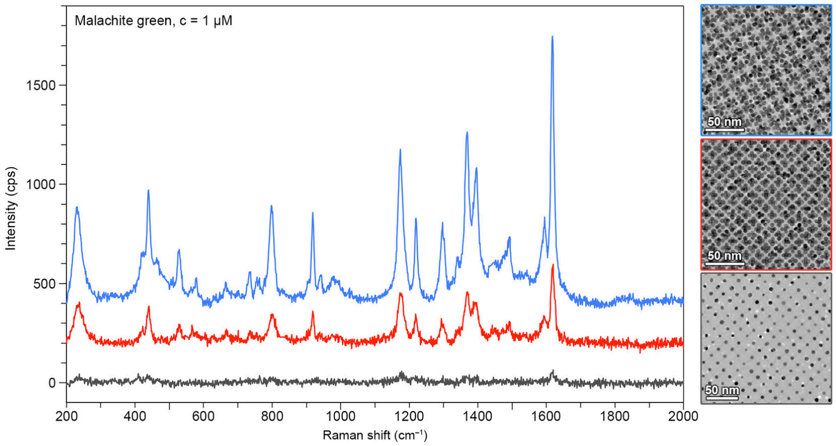

Fig. 4. SERS spectra of a model analyte—malachite green—recorded from three different NCP NP arrays shown in the TEM images: *vac*$_1$Au$_1$ (gray), *vac*$_1$Au$_5$ (red), and *vac*$_1$Au$_{11}$ (blue).

Supplementary Materials:

Materials and Methods

Supplementary Text

Figures S1-S52

Tables S1-S5

Caption for Database S1

Supplementary Materials for

Tunable porous nanoallotropes prepared from binary nanoparticle superlattices formed at liquid-air interfaces

Thumu Udayabhaskararao, Thomas Altantzis, Lothar Houben, Marc Coronado-Puchau,
Judith Langer, Ronit Popovitz-Biro, Luis M. Liz-Marzán, Lela Vuković, Petr Král,
Sara Bals, Rafal Klajn

Correspondence to: rafal.klajn@weizmann.ac.il

This PDF file includes:

- Materials and Methods
- Supplementary Text
- Figs. S1 to S52
- Tables S1 to S5
- Caption for Database S1

Materials and Methods

Colloidal synthesis of nanoparticles (NPs)

Synthesis of 5.2±0.4 nm gold nanoparticles: monodisperse 5.2 nm dodecanethiol-stabilized Au NPs were prepared based on a previously reported procedure (*31*). Specifically, 65 mg of $HAuCl_4 \cdot 3H_2O$ and 202 mg of didodecyldimethylammonium bromide (DDAB) were dissolved in 20 mL of toluene (with sonication). In a separate vial, 700 mg of $NaBH_4$ was dissolved in 2 mL of deionized water. Next, 100 µL of the borohydride solution was injected into the $AuCl_4^-$ solution with vigorous stirring. Neat dodecanethiol (DDT) (1.6 mL) was added and the mixture was stirred for an additional 2 h. The resulting solution was mixed with 20 mL of ethanol and DDT-passivated Au NPs were precipitated by centrifugation, collected, dried under vacuum, and then redispersed in a mixture of 20 mL of toluene and 1.6 mL of DDT (with sonication). Thus obtained solution was refluxed for 3 h under a nitrogen atmosphere (digestive ripening (*32*)). The solution was allowed to cool down and the NPs were precipitated with ethanol (with centrifugation). The precipitate was collected, dried under vacuum and redispersed in 5 mL of pure toluene. The resulting solution was centrifuged (5 min at 7,000 rpm) to remove any large particles; the upper layer was collected, dried under vacuum, and finally redispersed in pure hexane. TEM images of the resulting NPs are shown in Fig. S1, *left*.

Synthesis of 5.2±0.4 nm gold nanoparticles: The more polydisperse particles were obtained by storing the above 5.2±0.4 nm Au NPs in hexane for three months at room temperature. TEM images of the resulting NPs are shown in Fig. S1, *center*.

Synthesis of 3.0±0.3 nm gold nanoparticles: Monodisperse 3.0 nm dodecanethiol-stabilized Au NPs were prepared by modifying a previously reported procedure (*33*). First, a solution of 98.5 mg of $HAuCl_4 \cdot 3H_2O$ and 10 mL of oleylamine (OLA) in 10 mL of hexane was prepared and brought to 15 °C using a thermostatic bath (with magnetic stirring). To the resulting orange mixture, a solution of *t*-butylamine-borane complex (44 mg) in 1 mL of hexane containing 1 mL of OLA was injected under a nitrogen flow. The mixture turned purple within 5 s and was allowed to react at 15 °C for an additional hour before ethanol (60 mL) was added to induce the precipitation of the NPs. The NPs were collected by centrifugation (6,000 rpm for 5 min), washed with ethanol, dried, and redispersed in pure toluene. The particles were functionalized with DDT by place-exchange reaction as reported previously (*34*). Specifically, 10 eq of DDT (per surface-bound OLA) were added to the NPs and the mixture was shaken on an orbital shaker for 12 hours. The DDT-passivated NPs were purified from excess DDT by precipitation and copious washing with methanol, and finally redispersed in pure hexane. TEM images of the resulting NPs are shown in Fig. S1, *right*.

Synthesis of iron oxide nanoparticles: Iron oxide (Fe_3O_4) NPs (8.4±0.4 nm, 10.6±0.6 nm, 13.0±0.6 nm) were synthesized by modifying a previously reported literature procedure (*35*). First, iron(III) oleate was prepared as follows: to a solvent mixture composed of *i*) 60 mL of distilled water, *ii*) 80 mL of ethanol and *iii*) 140 mL of hexane were added sodium oleate (36.5 g; 120 mmol) (TCI, >97%; note that the high purity of sodium oleate was critical for reproducible synthesis of high-quality, monodisperse Fe_3O_4 NPs) and $FeCl_3 \cdot 6H_2O$ (10.8 g; 40 mmol) (Alfa Aesar, 98%) and the resulting mixture was vigorously stirred at room temperature until a homogeneous solution was obtained. The mixture was then heated with vigorous stirring under a nitrogen atmosphere at 70 °C for 4 hr. The solution was cooled down to room temperature and the upper phase (dark-red color) was collected using a separatory funnel and washed three times with distilled water. The resulting dark-red solution of iron oleate in hexane was dried over anhydrous magnesium sulfate. The solvent was evaporated *in vacuo* at 70 °C, resulting in a brown waxy solid. Next, iron oleate (1.60 g; 1.78 mmol) was dissolved in 25 mL of 1-octadecene (Aldrich, 90%) and a given amount of oleic acid (Alfa Aesar, 90%) was added. The amount of oleic acid controlled the diameter of the resulting NPs: to obtain 8.4 nm, 10.6 nm, and 13.0 nm Fe_3O_4 NPs, we added 1.1 g (3.90 mmol), 0.99 g (3.55 mmol), and 0.86 g (0.30 mmol) of oleic acid, respectively. The reaction mixture was initially heated to 80 °C under reduced pressure for 30 min in order to remove any low-boiling liquids, and subsequently heated up to T = 310 °C at a constant heating rate of 3 °C per min, and it was stirred at this temperature for 30 min under a nitrogen atmosphere. The heating mantle was removed and the reaction mixture was allowed to cool down to room temperature. Nanoparticles were purified by precipitating with a mixture of solvents composed of hexane, isopropanol, and acetone ($v/v/v$ = 1:2:2). The transparent supernatant was discarded and the solids were washed with a hexane-acetone mixture (v/v = 1:2). Residual solvent was evaporated under reduced pressure, resulting in monodisperse Fe_3O_4 nanoparticles as a black solid. The resulting oleate-passivated NPs were readily soluble in hexane. TEM images of as-prepared Fe_3O_4 NPs are shown in Fig. S2.

Fabrication and characterization of binary nanoparticle superlattices (BNSLs) and non-close-packed (NCP) NP arrays

Self-assembly of BNSLs: BNSLs were prepared based on a previously reported method (*20*). Hexane solutions of Au and Fe_3O_4 NPs were mixed to afford an Au/Fe_3O_4 particle ratio between 0.5 and 10. The resulting solution was diluted with pure hexane such that the total NP concentration was 0.1-1 mg/mL. Next, 10 µL of the diluted solution was dropcasted onto several mL of diethylene glycol (DEG) inside a Teflon well. The well was covered with a glass slide and hexane was allowed to evaporate within ca. 15 min. The resulting BNSLs were transferred onto carbon-coated copper grids or Si wafers for inspection by TEM and SEM, respectively.

Selective etching of BNSLs: BNSLs obtained at the DEG-air interface were transferred onto carbon-coated substrates using a lift-off technique. We worked with both commercial and homemade substrates. Homemade substrates were prepared as follows: copper grids (300- or 400-mesh) were covered with a thin film of nitrocellulose, prepared by spreading 3-4 drops of 1% solution of nitrocellulose in amyl acetate on the surface of water (in a crystallizing dish). The dried grids were then coated with a thin layer of amorphous carbon using an Edwards evaporator. Alternatively, commercial substrates (copper grids coated with amorphous carbon supported on Formvar; Electron Microscopy Sciences FCF400-CU-50) could be used. Residual DEG was removed by placing the substrates under high vacuum. The dried grids were subjected to heating (70 ºC in an oven, typically for 1-2 hr), placed inside a vacuum chamber of a TEM (we worked with a Philips CM120 Super Twin TEM operated at 120 kV), and exposed to the electron beam for 10-20 min in a low-magnification mode (such that the entire grid was exposed to the beam at once). The grids were removed from the TEM and placed in an etchant solution. For a selective removal of Fe_3O_4 NPs, we used a 3.5 M aqueous solution of HCl (etching time: 10-60 sec). For a selective removal of Au NPs, a 0.1 M aqueous solution of KCN was used (etching time:

30-60 min) (for etching of Au, pre-exposure to the electron beam was not required). The grids were rinsed with deionized water and finally dried under high vacuum.

Supplementary Text

Modeling of BNSLs at the liquid-air interface

We used classical atomistic molecular dynamics (MD) simulations to examine the principles governing the self-assembly of NPs at liquid-air interfaces. We determined the immersion of individual particles, calculated the energies associated with the immersion process, and found the NP-NP binding energies in vacuum and at the liquid-air interfaces.

Molecular dynamics simulations: Atomistic models of a dodecanethiol-covered Au NP (core diameter ~5 nm, 380 ligands) and an oleate-covered Fe_3O_4 NP (core diameter ~10 nm, 1270 ligands) were prepared (*40-42*). For simplicity, both types of NPs were modeled as hollow shells formed by atomic monolayers of icosahedral shapes with randomly attached ligands. These NPs were modeled alone or in pairs at the liquid-air interface (where liquid = diethylene glycol (DEG), ethylene glycol (EG), and water) and at the DEG-hexane interface. The systems contained between 30,000 and 700,000 atoms and were simulated for 15-100 nanoseconds.

MD simulations were performed with NAMD2.11 software (*43*). NP ligands and solvents were described with the generalized CHARMM force field (*44, 45*), and the parameters were determined via the CGenFF ParamChem web interface (*46, 47*). The NP core atom parameters had little influence on the NP-solvent and NP-NP interactions since they were densely covered by NP ligands. In all the simulations, the particle-mesh Ewald (PME) method (*48*) was used for evaluation of long-range Coulomb interactions. The time step was set to 2.0 fs, and long-range interactions were evaluated every one (van der Waals) or two (Coulombic) time steps. After 2,000 steps of minimization, solvent molecules were equilibrated for 1 ns around the NPs, which were restrained using harmonic forces with a spring constant of 1 kcal/(mol Å^2). Then, the systems were equilibrated by MD simulations without restraints. The simulations were performed in the NpT (DEG-hexane interface; p = 1 bar) and NVT ensembles (all vacuum interfaces) at a constant temperature of T = 310 K and a Langevin constant of $\gamma_{Lang} = 0.01$ ps^{-1}.In order to quantify the binding affinity of NPs to different liquids and their interfaces, NAMD Energy plugin in VMD (*49*) was employed. Images of the simulated systems were also prepared with VMD. All the analyses were performed during second halves of production runs.

Gibbs free energy calculations: Gibbs free energy of binding between a single DEG molecule and a gold NP in vacuum was determined in umbrella sampling (US) calculations (*50*). The reaction coordinate, defined as the distance between the center of mass of a DEG molecule and the NP core center was partitioned into 17 windows of a 1-Å width. Confinement potentials were introduced in the form of harmonic restraints with a force constant k = 3 kcal/(mol Å^2) and each window was run for 10 ns as the DEG molecule quickly sampled its binding conformations. The weighted histogram analysis method (WHAM) was used to reconstruct the PMF, and Monte Carlo bootstrap error analysis was performed also with the WHAM algorithm (with num_MC_trials set to 5) (*51, 52*). The histograms of the US windows used to reconstruct the PMF were examined, and had an appropriate overlap.

Single NPs at interfaces: In the first set of simulations, individual Au and Fe_3O_4 NPs (described above) were placed at midpoints of the DEG-hexane, DEG-vacuum, EG-vacuum, and water-vacuum interfaces. Fig. S48 shows that during the equilibration simulations

NPs adjusted to their preferred solvation levels at these interfaces. At the DEG-hexane interface, Au NPs and Fe_3O_4 NPs immersed into hexane within 50-70 nanoseconds (Fig. S48A). At the DEG-vacuum and EG-vacuum interfaces, both Au NPs and Fe_3O_4 NPs remained about halfway immersed in the liquids during 50 nanoseconds of simulations (Figs. S48A and S48B). At the water-vacuum interface, both types of NPs shifted towards vacuum within 15 nanoseconds, thus reducing the ligand-water contact area (Fig. S48D).

Table S1 provides the coupling energies between individual Au or Fe_3O_4 NPs and the underlying liquids (DEG, EG, and water). The coupling energies were calculated by the VMD plugin that provides the sum of van der Waals (vdW) and Coulombic coupling energies between the NP ligands and the solvent molecules (determined by parameters in the CHARMM force field), which are related to the respective forces (vdW: attractive; steric: repulsive; Coulombic: both attractive and repulsive) acting between the system's components. These energies only represent partial (see below) enthalpy components in the Gibbs free energies of NPs binding to the underlying liquids. For simplicity, we can assume that the Gibbs free energies are proportional to these enthalpies with a common factor. Simplified calculations performed below provide an estimate that the Gibbs free energies can be about 2-3 times smaller than these enthalpies, due to the molecular confinement (entropic effects).

The calculations below show that the coupling energies of Au or Fe_3O_4 NPs to DEG are roughly proportional to the immersed areas of these NPs. Therefore, during the self-assembly processes, these NPs should have the ability to displace each other from the surface of DEG. In the case of EG, however, the coupling energies are not proportional to the immersed surfaces of NPs; rather, EG favors interactions with Fe_3O_4 NPs. Therefore, these NPs should dominate at the surface of EG and hence disrupt the NP co-assembly processes. These considerations are in agreement with previous experimental studies, which found that DEG is superior to EG in the formation of BNSLs (*26, 27*).

$$\text{DEG:} \qquad \frac{E_{\mathrm{Fe_3O_4}}}{E_{\mathrm{Au}}} = 3.67 \approx \frac{A_{\mathrm{Fe_3O_4}}}{A_{\mathrm{Au}}} = \frac{r^2_{\mathrm{Fe_3O_4}}}{r^2_{\mathrm{Au}}} = \frac{6.8^2}{3.6^2} = 3.57$$

$$\text{EG:} \qquad \frac{E_{\mathrm{Fe_3O_4}}}{E_{\mathrm{Au}}} = 4.38 > \frac{A_{\mathrm{Fe_3O_4}}}{A_{\mathrm{Au}}} = \frac{r^2_{\mathrm{Fe_3O_4}}}{r^2_{\mathrm{Au}}} = \frac{6.8^2}{3.6^2} = 3.57$$

NP pairs at the DEG-vacuum interface: In the second set of simulations, coupling energies of pairs of NPs (Au-Au, Au-Fe_3O_4, and Fe_3O_4-Fe_3O_4) (evaluated by VMD) were examined in vacuum and at the DEG-vacuum interface. Initially, the NPs were placed close to each other. After 30-40 ns of simulations, the separation between the NPs decreased both in vacuum and at the DEG-vacuum interface as the ligands on the different NPs reached each other and started to interact very strongly. At the DEG-vacuum interface, the NPs immersion levels remained similar as at the beginning of the simulations (about half-immersed).

In Table S2, we provide the NP-NP coupling energies (enthalpies), calculated as in Table S1, for the cases shown in Fig. S49. One can see that the interparticle interactions at the DEG-vacuum interface (–200 to –440 kcal/mol) are weaker than in vacuum (–250 to –480 kcal/mol) since the ligand-ligand coupling between the neighboring NPs is partly replaced by the ligand-DEG coupling. This weakening of the NP-NP coupling for submerging

NPs explains why the relatively weak bulk vdW coupling between the NP cores (~ –5 kcal/mol) becomes important only for NPs fully immersed in DEG. Indeed, if the strengths of the ligand-DEG coupling and the ligand-ligand coupling were similar, the ligands would not contribute to the binding of submerged NPs (i.e., the ligand-related enthalpic component in the Gibbs free energy of NP-NP binding would be ~0). These results also show that i) the evaporation of hexane dramatically increases the NP-NP coupling (it "locks" the NPs) and ii) the NP-liquid coupling can become dominant owing to the large contact area formed between DEG and half-submerged NPs.

NPs favor semi-immersed positions at the DEG-vacuum interface: In order to explain why NPs assume semi-immersed positions at the DEG-vacuum interface (see Figs. S48, S49), we examined the major energetic contributions to NP solvation. When a NP immerses in a liquid, it creates a cavity with an excess surface area of the solvent, A_{excess}. The Gibbs free energy cost, G_1, to create the additional surface area in DEG can be estimated as, $G_1 = \gamma\ A_{excess} = \gamma\ (A_{immersed} - A_{slice}) = \gamma\ (2\pi Rh - \pi(2Rh - h^2))$, where γ is the surface tension of DEG (~45 dyne/cm), surface areas are defined as in Fig. S50A, R is the radius of the ligand-functionalized Au NP (i.e., NP core + ligand shell) estimated as 3.5 nm, and h is the immersion height of the NP. The free energy cost of submerging a gold NP, G_1, as a function of NP immersion depth, h, is shown as the red line in Fig. S50B.

The Gibbs free energy cost of creating the cavity is balanced by favorable interactions between the NP ligands and the solvent, which can be estimated as $G_2 = G° A_{immersed}$, where G° is the free energy per unit area of binding between DEG and a gold NP, and $A_{immersed}$ is shown schematically in Fig. S50B. For a dodecanethiol-covered Au NP, we can estimate $G° \sim -7$ kcal/(mol nm^2) from the Gibbs free energy of binding of a single DEG molecule to Au NP, $\Delta G_{bind} = -3.5$ kcal/mol, and the approximate contact area that a DEG molecule has with the Au NP surface (0.5 nm^2) (Fig. S50C). The interaction energy, G_2, as a function of the immersion height, h, is shown as the blue line in Fig. S50B. The Gibbs free energy, G_2, is about 2-3 times smaller than the energy (enthalpy), E_2, directly obtained from our simulations (VMD), highlighting the importance of the entropic contribution.

By adding the two Gibbs free energy contributions, G_1 and G_2, we obtain the total free energy, G, as a function of the immersion height, h, which is shown as the black line in Fig. S50B. The energy cost, G_1, increases and the favorable free energy of DEG-NP binding, G_2, decreases as the NP immerses into DEG. Overall, the total free energy develops a minimum at an approximately half-immersed position of the Au NP in DEG, as observed in equilibrium MD simulations.

BNSLs prepared at DEG/water-air interfaces: To further confirm the unique role of DEG in templating the formation of well-ordered BNSLs, we studied self-assembly of a 1:1 mixture of ~5 nm Au and ~10 nm Fe_3O_4 NPs in the presence of several DEG/water mixtures. We found that the presence of as little as 10% (*v*/*v*) water in the underlying liquid had a profound deleterious effect on the quality of the BNSL obtained. Instead of a well-defined NaCl-type monolayer (Fig. S51A), we observed the formation of a ~1:1 mixture of the monolayer and the "type II" bilayer (Fig. S51B). The formation of bilayers from NPs used in amounts expected to give rise to submonolayer coverage of the underlying liquid indicates a weaker coupling to the liquid and consequently a greater contribution of the NP-NP coupling. This effect was more pronounced in the presence of 25% water, where we found the formation of both types of NaCl-type bilayers, in addition to thicker BNSLs (Fig. S51C). A small fraction of monolayer coverage was still present. When self-assembly took place on a 1:1 (*v*/*v*) DEG-water mixture, no monolayers could be found; instead, thick arrays comprising several NP layers prevailed. Under these conditions, we also observed quasi-3D superlattices composed only of Fe_3O_4 NPs (Fig. S81D). Overall, these observations are in agreement with the results of our simulations (Fig. S48D), which show poor coupling of both types of NPs to water compared to DEG.

Lattice energies of BNSLs: The NP-NP interaction energies displayed in Tables S1 and S2 can be used to estimate the lattice energies of the experimentally observed BNSLs. In these calculations, we first identify, based on the structural models shown below, the smallest repeating unit of each BNSL in the x-y plane (parallel to the liquid-air interface), which we define as the square whose corners are located to the centers of neighboring Fe_3O_4 NPs. In the z-direction (perpendicular to the liquid-air interface), we consider the initial two layers comprising Fe_3O_4 NPs. Then, we determine the number of Au and Fe_3O_4 NPs per unit cell that are in contact with DEG and multiply them by the NP-DEG coupling energies calculated above (Table S1). Next, we determine the number of interparticle contact points (i.e., Au-Au, Au-Fe_3O_4, and Fe_3O_4-Fe_3O_4) within the unit cell and multiply them by the NP-NP interaction energies (Table S2). For the base NP layers, the NP-NP interaction energies were divided by two since their bottom hemispheres were immersed in DEG and the NP-DEG interaction was separately accounted for (Table S1). The obtained total energies (enthalpies) are listed in Table S3 for three selected BNSLs sharing the same AB_4 bottom layer: AB_4 (i.e., $(-AB_4-)_n$), AB_6 (i.e., $(-AB_4-B_2-)_n$), and AB_{11} (i.e., $(-AB_4-B_7-)_n$).

These considerations confirm the profound role of NP-DEG interactions on the stability of the resulting BNSLs. For example, the calculated coupling energy between the base layer of NPs in the AB_6-type BNSL and DEG is ~9,250 kcal/mol per unit cell, which is roughly an order of magnitude higher than the interaction energy between two adjacent monolayers of NPs (held together by four Au-Au contacts per unit cell; ~1,000 kcal/mol). Therefore, coupling to DEG plays a key role in controlling the formation of BNSLs. It should be emphasized, however, that these estimations are only approximate because: i) the NP-NP coupling energies were calculated for energy-minimized configurations of individual pairs of NPs, which does not reflect the situation in ensembles of multiple regularly arranged NPs; ii) both Au and Fe_3O_4 NPs used in the experiments were slightly polydisperse and their sizes and size ratios in the BNSLs could be different from the 5 nm and 10 nm sizes used in simulations.

Immersion of multilayer superlattices in DEG: Having established that monolayer-thick superlattices prefer to assume a half-immersed configuration at the DEG-vacuum interface, we studied the behavior of thicker superlattices by comparing the NP solvation forces with the gravitational forces acting on the superlattices. In particular, we were interested in determining at which value of superlattice thickness, its bottom layer becomes fully immersed.

Figure S52A shows our estimate of forces ($F_{immerse}$) associated with the immersion of a single dodecanethiol-functionalized Au NP (5 nm core + 1 nm ligand shell) positioned at the DEG-vacuum interface, derived from the free energy plot in Fig. S50B. The net force can be obtained by differentiating the free energy of NP solvation with respect to the immersion height. The free energy of solvation is defined as the sum of the energy cost term (creating the additional solvent interface upon immersion) and the favorable energy term (favorable ligand-DEG interactions upon NP immersion). When a nanoparticle is equilibrated at the DEG-vacuum interface, it is approximately half-immersed in DEG, so that a zero net force acts on it. When the NP is less than half immersed, a negative net vertical force pulls it into the DEG. When, on the other hand, the NP is more than half immersed, a positive net vertical force pulls it out of DEG. We estimate that a vertical force of $F_{immerse} \sim 1.05 \cdot 10^{-9}$ N = 1.05 nN needs to be applied on this NP to fully immerse it into DEG. In contrast, a gravitational force acting on such a NP (mass of $\sim 2.2 \cdot 10^{-21}$ kg), $F_{grav} \sim -2.2 \cdot 10^{-20}$ N, is eleven orders of magnitude smaller. Although this force cannot lead to full immersion of the NP, a superlattice comprising many self-assembled NPs could have a different balance of forces.

Next, we examined the possible immersion of two model NP superlattices shown in Fig. S52B and C. First, we studied a cubic superlattice formed by spherical NPs (Fig. S52B), similar to that observed experimentally. Here, DEG could fill the space between the NPs from the bottom superlattice layer. Therefore, each of these bottom-layer NPs opposes its immersion beyond the equilibrium (~half-immersion) level by a force that stabilizes the whole superlattice from immersion. The solvation forces acting on each of these spherical NPs can be determined using the approach shown in Figs. S50B and S52A. For example, when a bottom-layer NP is 60% immersed in DEG, the opposing immersion force acting on it is $F_{immerse} \sim 2.18 \cdot 10^{-10}$ N (Fig. S52A).

Based on the above estimates and assuming that the solvent level is flat, we determined the minimum forces needed to fully submerge the bottom (base) layers of superlattices formed by spherical NPs; see Table S4. If the linear size of these base layers is increased by a factor of 10, the force required to submerge them is correspondingly increased by a factor of 100. By balancing $F_{immerse}$ with F_{grav} for each selected base layer, we can determine how tall the superlattices would need to be in order to submerge their bottom layer into the underlying DEG phase. The calculated height of the supported NP column is 70.6 m (even for 60% immersion) regardless of the base layer size. This large value shows that DEG practically cannot enter the superlattice, which behaves more like a compact body lacking pores. Therefore, we assume that superlattice immersion is controlled by the interactions of its side NPs with the solvent, which will more or less surround the immersed part of the superlattice, while staying within the first NP monolayer. Since the bottom-edge NPs might be more surrounded by the solvent, their NP-NP coupling should be weakened; therefore, these NPs might be released, resulting in a superlattice with smoother bottom edges.

To provide an estimate of the supporting forces, we can simplify the system by considering a more compact NP superlattice, where the solvent has limited access to the NPs. Such a case is shown in Fig. S52C, where a superlattice is prepared from tightly packed cubic NPs (nanocubes, NCs) with an edge length of 7 nm (by analogy to spherical NPs having a 7 nm diameter). Here, the solvent is only present outside the superlattice, which means that only the external periphery of the superlattice contributes to its support against immersion. It turns out that when one of the NC facets is parallel to the solvent surface, the NCs can exist in two limiting solvation states, depending on the value of the ligand-DEG binding free energy. For ligand-DEG binding energies smaller than a certain threshold value, only the bottom NC facet interacts with DEG, whereas above the threshold value, the NCs become completely immersed, except for their top facets. This behavior is also valid for cubic assemblies of NCs shown in Fig. S52C. In order to have individual NCs floating (i.e., not submerged), we considered in our calculations a model ligand-DEG free energy of binding, where $G° \sim -4.7$ kcal/(mol nm^2), corresponding to the value reported in Fig. S50 and scaled by 2/3.

Table S5 shows the solvation and gravitational forces acting on supercubes of increasing sizes, formed by self-assembled NCs (Fig. S52C), present at the DEG-vacuum interface. Here, as the edge length of the square base layer that faces the solvent increases by 10 times, the force required to immerse the system, $F_{immerse}$, increases by the same amount. By balancing $F_{immerse}$ with F_{grav} for each selected cubic base layer, we can determine how tall the superlattice should be to get immersed into DEG. For short edge lengths of the square base layer (< 0.5 μm), the superlattices must have a macroscopic height (> 0.68 m) to become immersed into DEG. In contrast, superlattices with much larger edge lengths of the square based layer (here, 500 μm) are immersed already when they reach mesoscale heights (680 μm). Based on Tables S4 and S5, we expect that superlattices assembled from $\sim 10^{11}$ NPs at the DEG-hexane interface are not able to immerse into DEG due to supporting NP-DEG coupling forces, but that larger systems would submerge like non-porous rigid bodies, depending on their overall sizes and densities (Archimedes' law).

Surface-enhanced Raman scattering

Surface-enhanced Raman scattering (SERS) measurements were performed with a confocal Raman microscope (InVia Reflex, Renishaw) equipped with a motorized scan stage, 633 nm laser excitation source (nominal output 16 mW), a corresponding laser line rejection filter (edge) and lens set, diffraction grating of 1,800 grooves/mm, and a Peltier-cooled CCD detector (size 512x1,024 pixels). The laser power was attenuated by means of neutral density filters in preset steps. Next, 3 mL of a 1 mM Malachite green ethanolic solution (freshly prepared from a 1 mM ethanolic stock) were dropcasted onto the TEM grids containing the three different porous nanoallotropes: *vac*$_1$Au$_1$, *vac*$_1$Au$_5$, and *vac*$_1$Au$_{11}$. Immediately after having been dried, the SERS spectra were measured in a 180° back-reflection geometry through a x100 magnification objective (Leica, numerical aperture 0.85) with an integration time of 10 s (extended scan mode) and a laser power of 40 mW at the samples at five different positions outside the copper grid. The collected spectra were averaged, smoothed (Savitsky-Golay method), and background-corrected using Wire 3.4 software.

The SERS activity of the three different substrates was measured by drop casting a solution of a dye Malachite green (MG) directly on the TEM grid. The characteristic SERS signals of MG (1617, 1594, 1393, 1366, 1298, 1218, 1173, 915, and 798 cm^{-1}) were obtained for structures *vac*$_1$Au$_{11}$ and *vac*$_1$Au$_5$, the former yielding ca. three times higher intensity. Interestingly, this intensity difference can be directly related to the number of available hotspots – analysis of tomography data revealed the presence of 28-32 nanogaps (defined as interparticle distances smaller than 1 nm) per 1,000 nm^2 of the *vac*$_1$Au$_5$ array, whereas for the *vac*$_1$Au$_{11}$ array, we found 78-85 nanogaps / 1,000 nm^2. As expected, sample *vac*$_1$Au$_1$ did not display any SERS signal owing to the significant separation distance between individual NPs, which prevents hotspot formation.

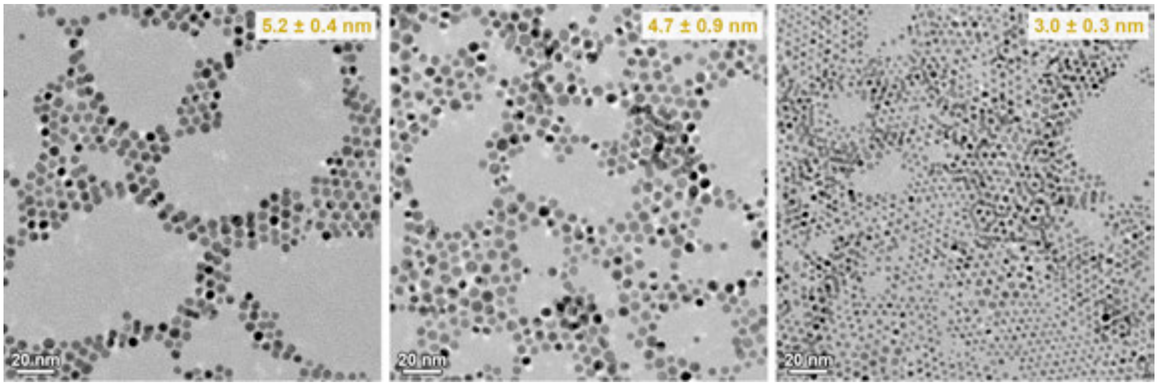

Fig. S1.

TEM images of gold nanoparticles used in the self-assembly experiments. To acquire TEM images, we used a Philips CM120 Super Twin TEM operated at 120 kV unless indicated otherwise.

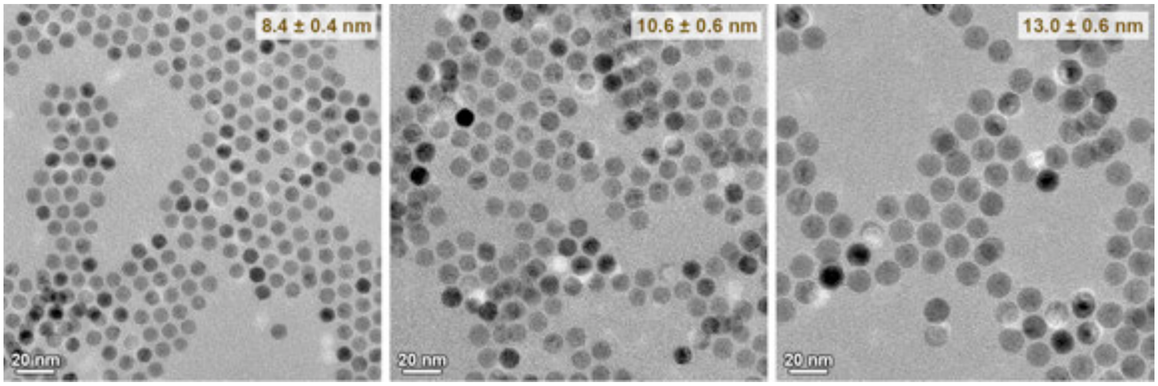

Fig. S2.
TEM images of iron oxide nanoparticles used in the self-assembly experiments.

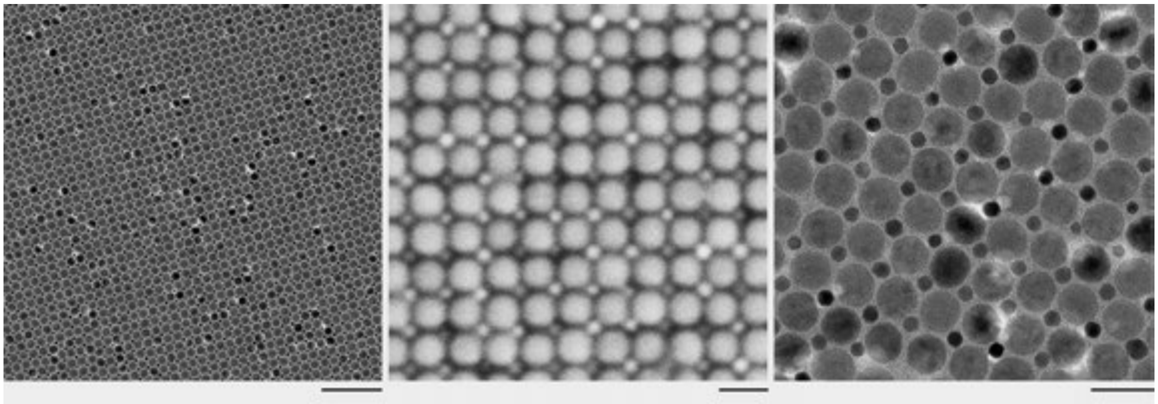

Fig. S3.

TEM and SEM images of a monolayer of an AB-type BNSL isostructural with the rock salt (NaCl) (*1, 22, 36*). The scale bars correspond to (L to R) 100 nm, 20 nm, and 20 nm. SEM images in our studies were acquired on an ULTRA 55 field-emission SEM or a SUPRA 55VP field emission SEM (both Carl Zeiss Microscopy, LLC), both operated at 5 kV.

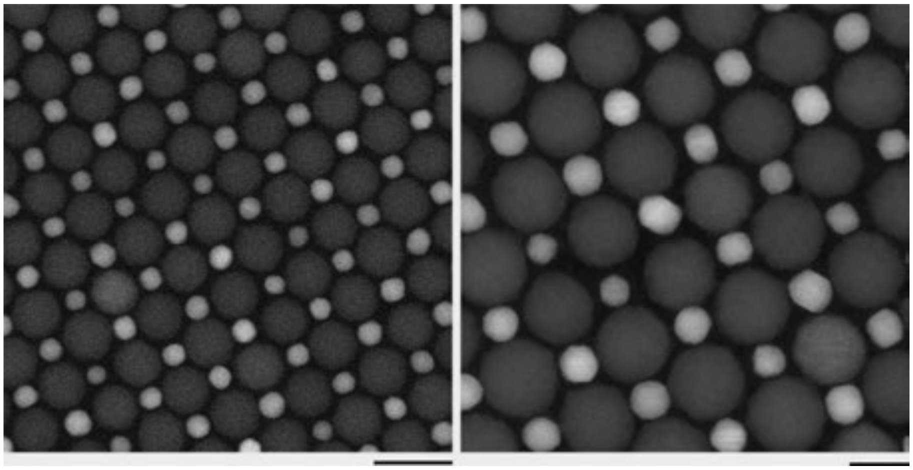

Fig. S4.

HAADF-STEM images of an AB-type BNSL. The scale bars correspond to 20 nm (left) and 10 nm (right). HAADF-STEM images in our studies were acquired on an aberration-corrected ‘cubed’ FEI-Titan electron microscope operated at 300 kV.

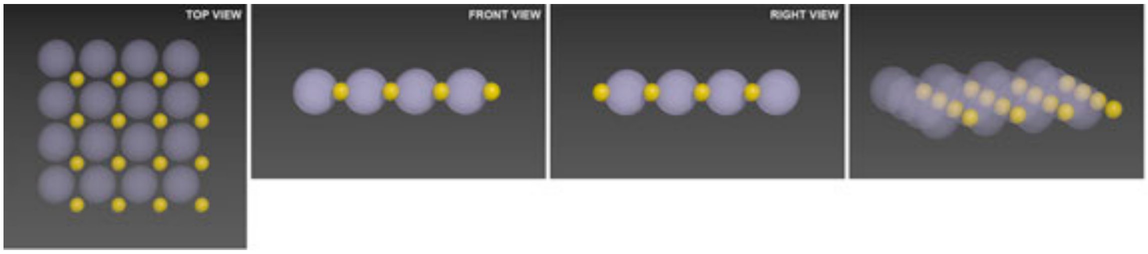

Fig. S5.

Structural model of the *vac*$_1$Au$_1$-type array. In this and the subsequent models, the filled yellow spheres represent Au NPs and the semi-transparent purple spheres represent vacancies corresponding to the positions of etched Fe_3O_4 NPs.

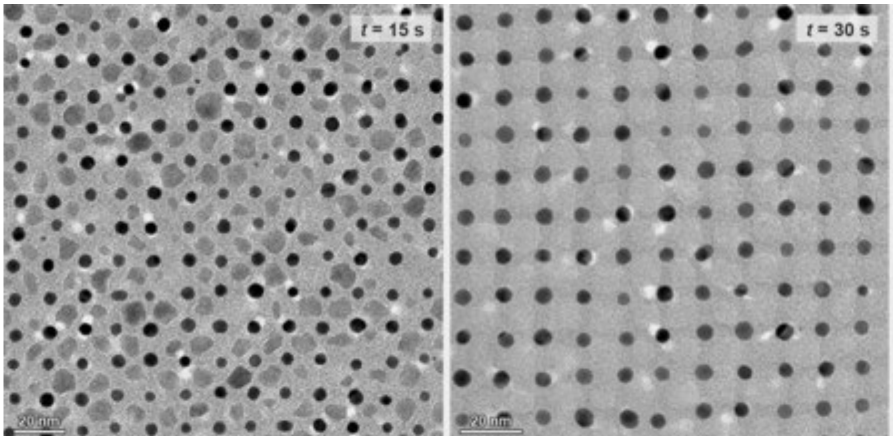

Fig. S6.

Following etching on carbon-coated nitrocellulose. Here, an AB-type BNSL was immersed into an aqueous HCl solution for 15 s (left) and 30 s (right).

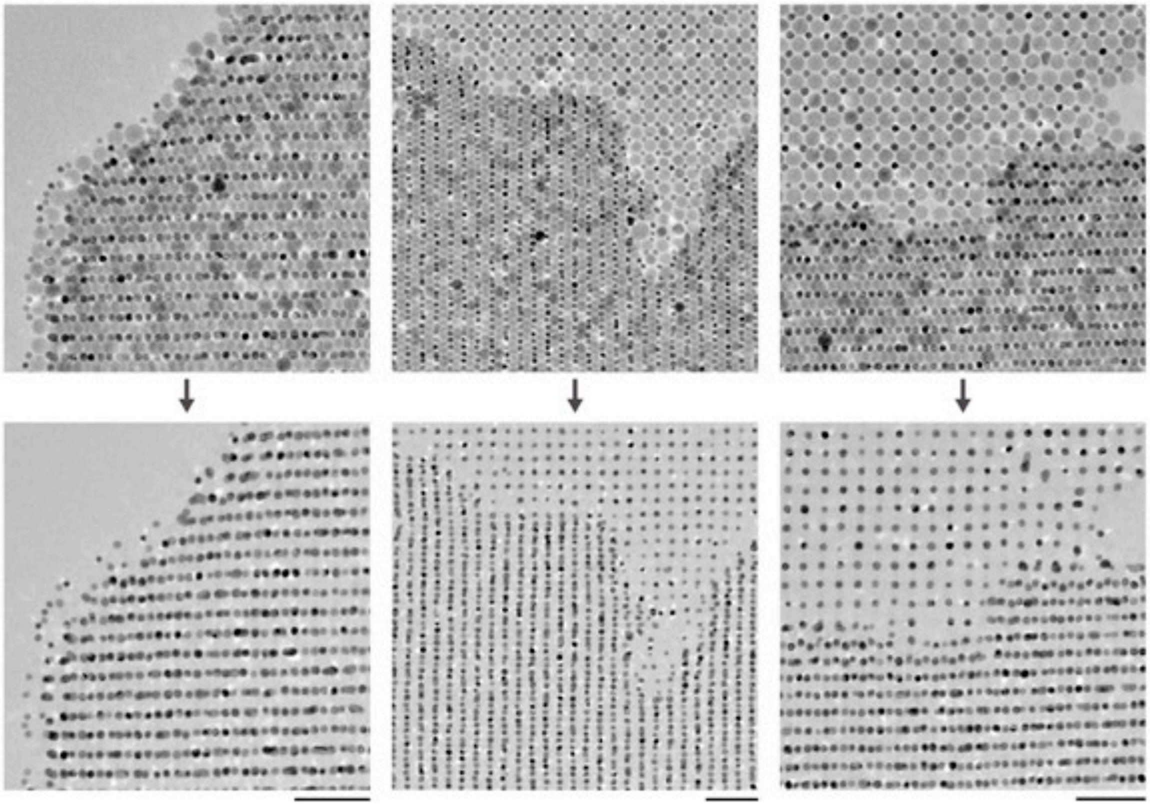

Fig. S7.

Additional examples of selective etching of Fe_3O_4 NPs with HCl without the disturbance of Au NPs. For clarity, we intentionally focused on the edge of the BNSL or regions containing defects. The scale bars correspond to 50 nm.

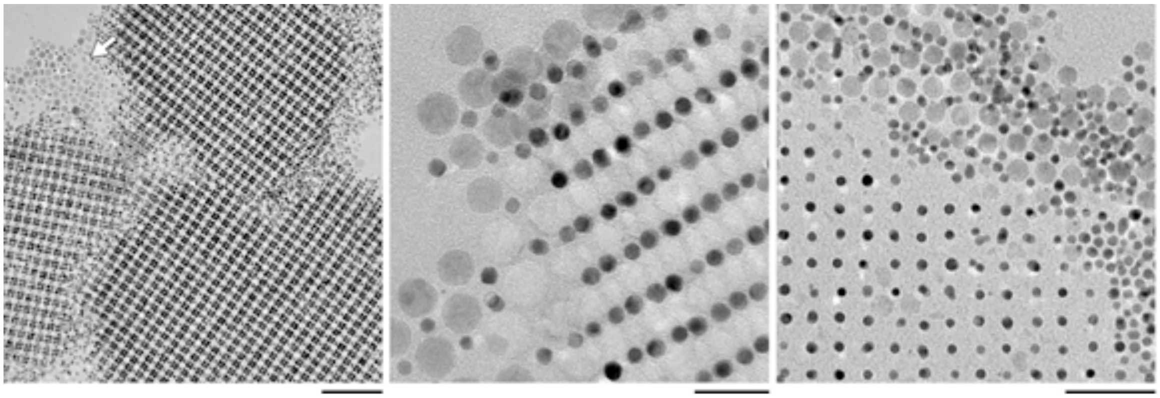

Fig. S8. Preferential etching of ordered arrays

The arrow in the image on the left points at unetched, disordered Fe_3O_4 NPs. In contrast, no residual Fe_3O_4 can be seen within ordered arrays. Preferential etching within ordered arrays can be explained by the particles having lost their protective organic coating. These observations suggest that regular arrangement of the NPs facilitates ligand desorption during mild thermal treatment. The scale bars correspond to (L to R) 100 nm, 20 nm, and 50 nm.

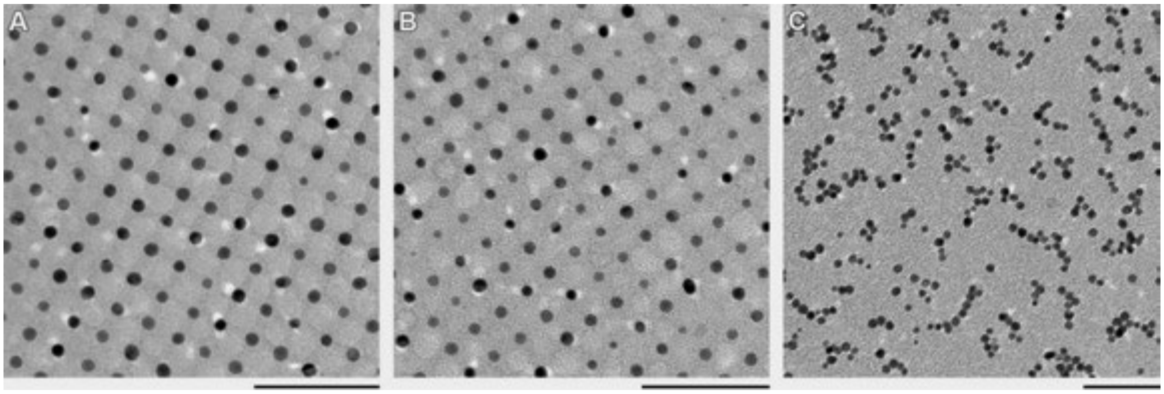

Fig. S9. Effect of the underlying substrate on the fixation of the NPs

An AB-type BNSL was deposited onto a homemade carbon-coated nitrocellulose film (left), a commercial carbon-coated Formvar film (center), and a nitrocellulose film lacking the carbon coating (right). Following thermal treatment under the same conditions, the BNSLs were treated with aqueous HCl. The scale bars correspond to 50 nm.

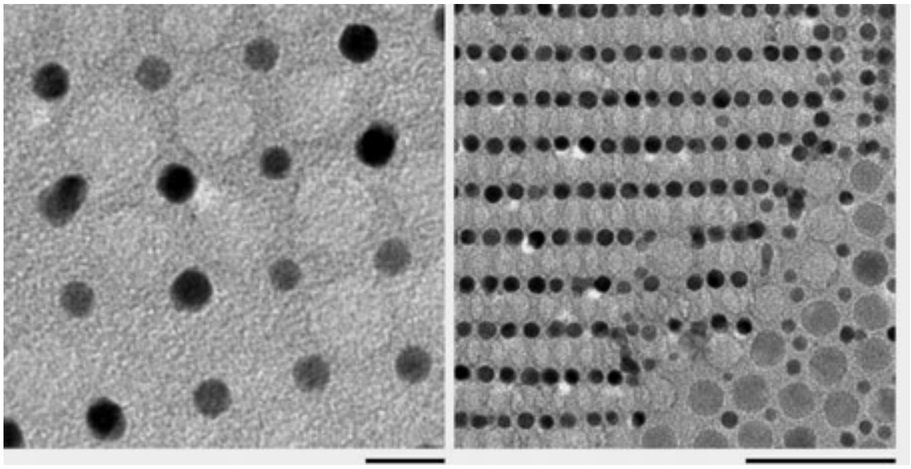

Fig. S10.

Residual carbonaceous films (seen in low contrast) observed after thermal treatment of AB-type BNSLs followed by etching with aqueous HCl. The films immobilize the Au NPs onto the underlying amorphous carbon film. The scale bars correspond to 10 nm (left) and 50 nm (right).

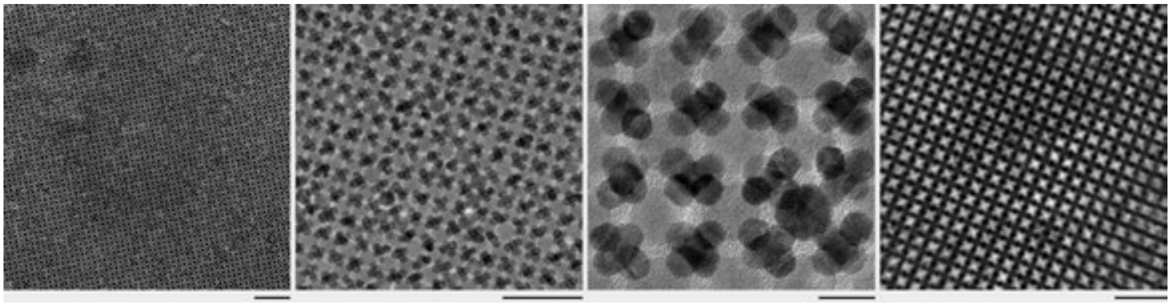

Fig. S11.

TEM images of an AB_6-type BNSL (lacking the top layer of Au NPs; the image on the right is a HAADF-STEM image taken using an FEI (Philips) Tecnai T12 operated at 120 kV). The scale bars correspond to (L to R) 100 nm, 50 nm, 10 nm, and 50 nm.

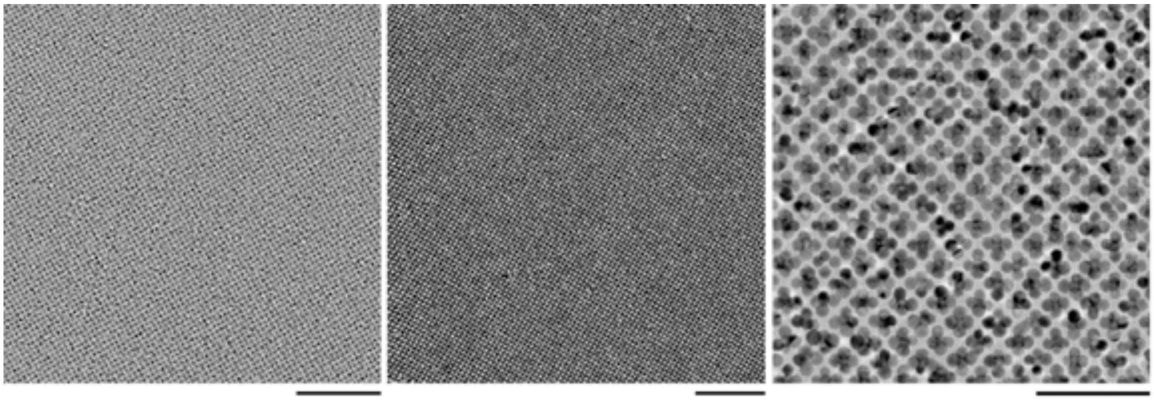

Fig. S12.

TEM images of a vac_1Au_5-type array. The scale bars correspond to (L to R) 200 nm, 200 nm, and 50 nm.

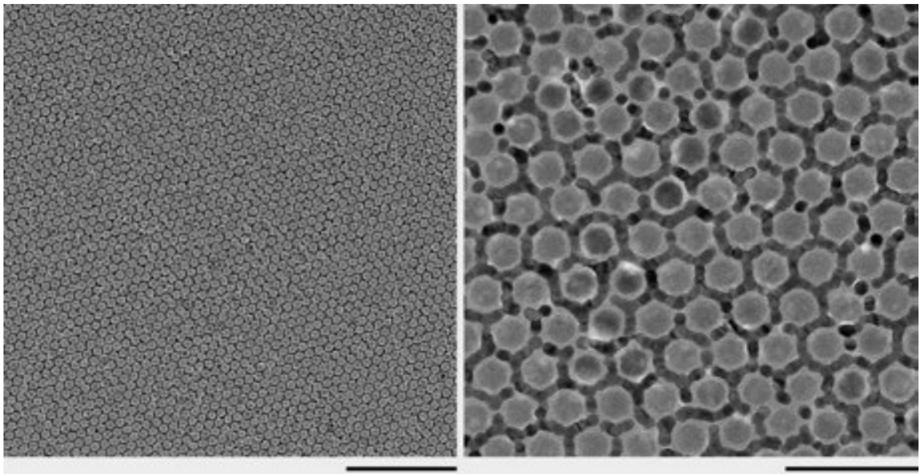

Fig. S13.

TEM images of a $CaCu_5$-type (*22, 37, 38*) BNSL (the [001] projection). This type of BNSL was occasionally found to coexist with the AB_6-type BNSL shown in Fig. 2A (see also Fig. S15 below). The scale bars correspond to 200 nm (left) and 50 nm (right).

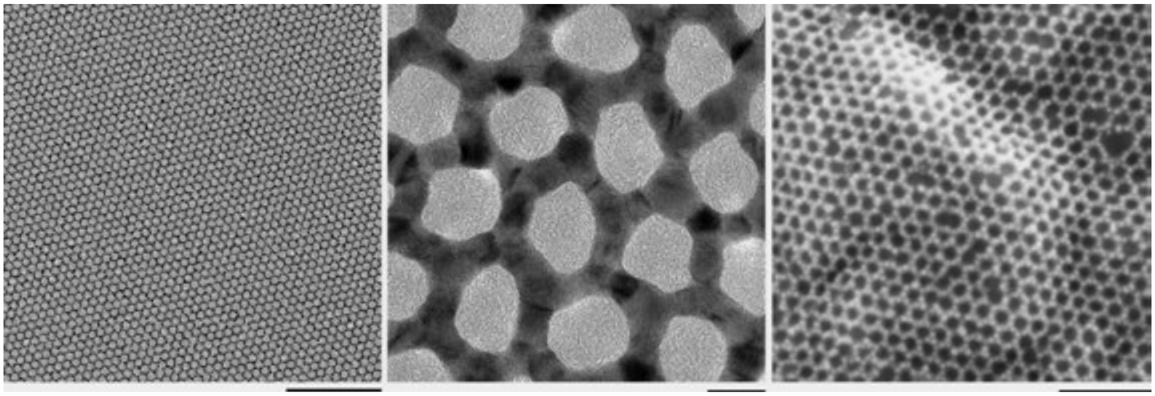

Fig. S14.

TEM (left, center) and SEM (right) images of honeycomb membranes obtained by thermal treatment and HCl etching of the $CaCu_5$-type BNSLs shown in Fig. S13. The scale bars correspond to (L to R) 200 nm, 10 nm, and 100 nm.

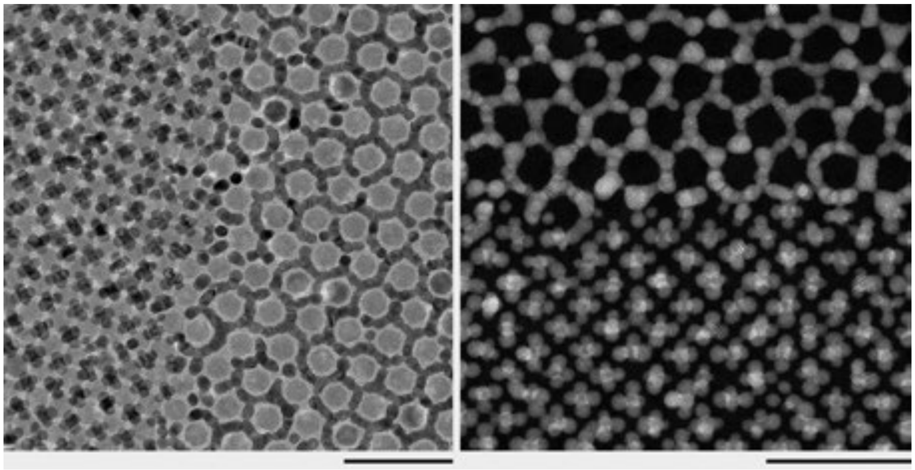

Fig. S15.

TEM (left) and HAADF-STEM (right) images showing an epitaxial relationship between the $CaCu_5$-type BNSL and the AB_6-type BNSL (shown in Fig. 2A). The STEM image was recorded after HCl etching. The scale bars correspond to 50 nm.

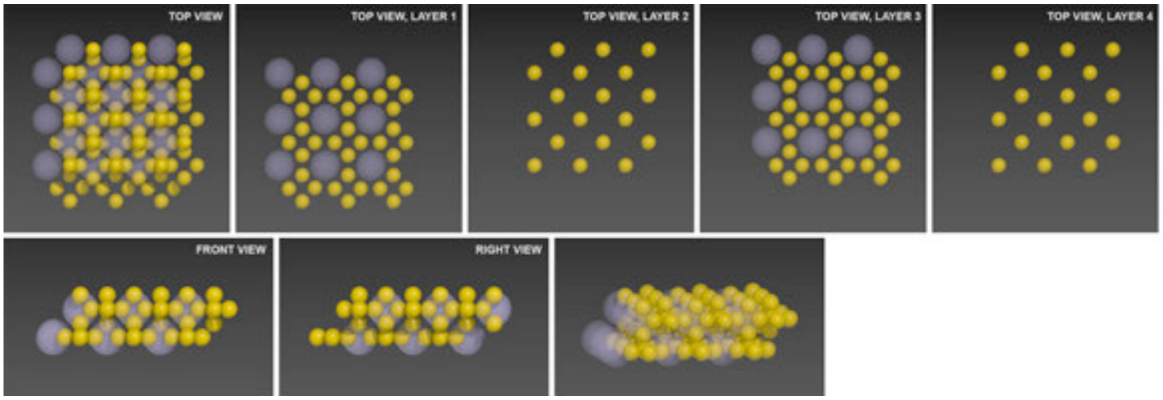

Fig. S16.

Structural model of the *vac*$_1$Au$_6$-type array.

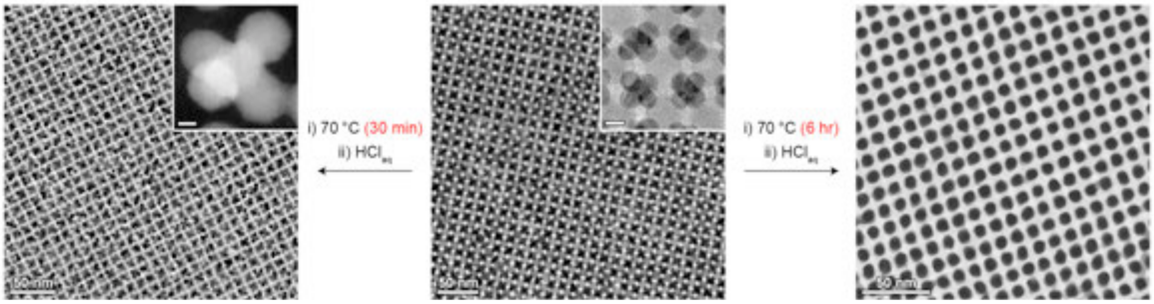

Fig. S17.

Effect of heating time on the morphology of the non-close-packed NP array obtained from the AB_6-type BNSL (here, lacking the top layer of Au NPs). The scale bars in the insets correspond to 5 nm (center) and 2 nm (left).

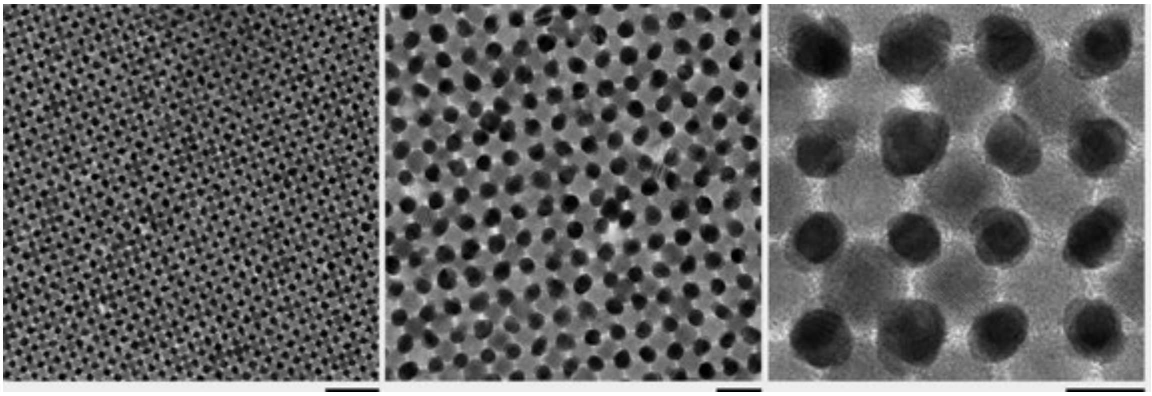

Fig. S18.

TEM images of an AB-type BNSL obtained by heating the AB_6-type BNSL (lacking the top layer of Au NPs) at 70 °C for 4 hours. The scale bars correspond to (L to R) 50 nm, 20 nm, and 10 nm.

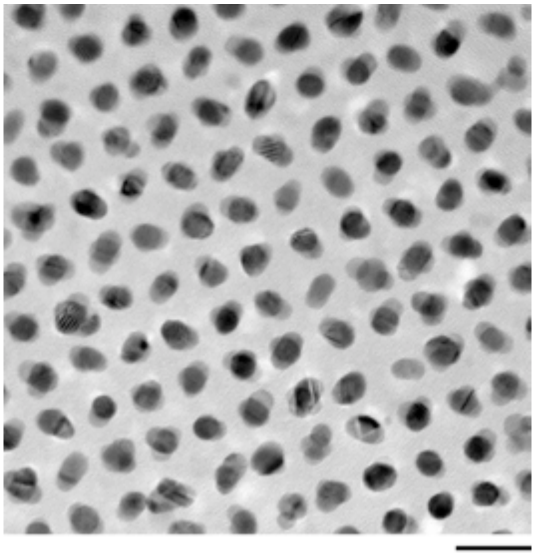

Fig. S19.

TEM image of an array of partially sintered clusters of Au NPs obtained by etching the BNSLs shown in Fig. S18. The scale bar corresponds to 20 nm.

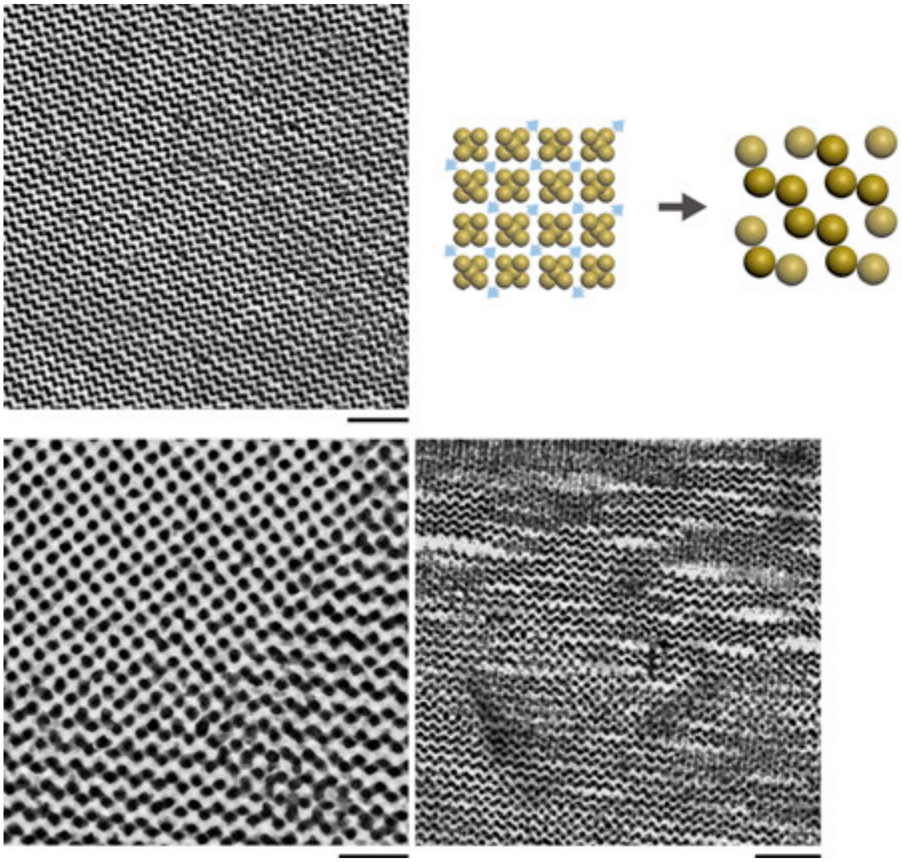

Fig. S20.

TEM images of zigzag-type nanowires obtained by simultaneous translation and coalescence of clusters of Au NPs as shown in the scheme in the top right (we found that this transformation was facilitated in the presence of oleic acid present in the system). The scale bars correspond to 100 nm (top), 50 nm (bottom left) and 100 nm (bottom right).

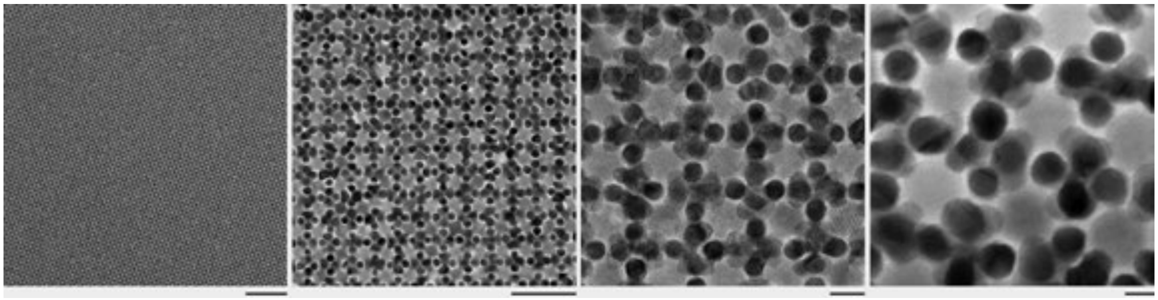

Fig. S21.

TEM images of an AB_{11}-type BNSL, where the top layer of Au NPs consists of Au quartets. The scale bars correspond to (L to R) 200 nm, 50 nm, 10 nm, and 5 nm.

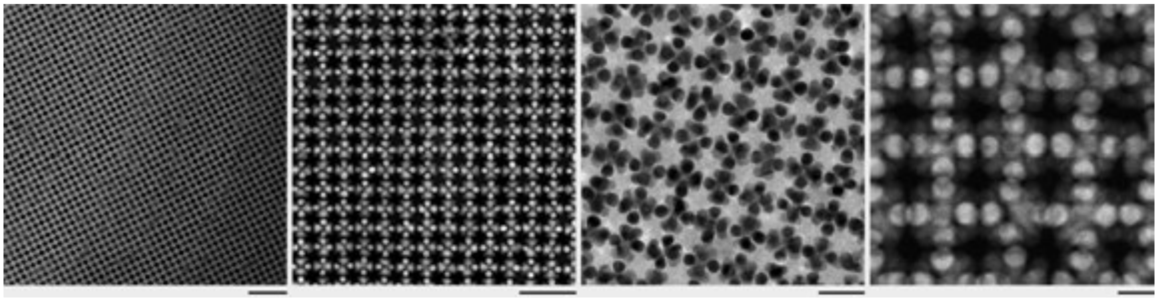

Fig. S22.

HAADF-STEM and TEM images of vac_1Au_{11}-type arrays, where the top layer consists of Au quartets. The scale bars correspond to (L to R) 100 nm, 50 nm, 20 nm, and 10 nm.

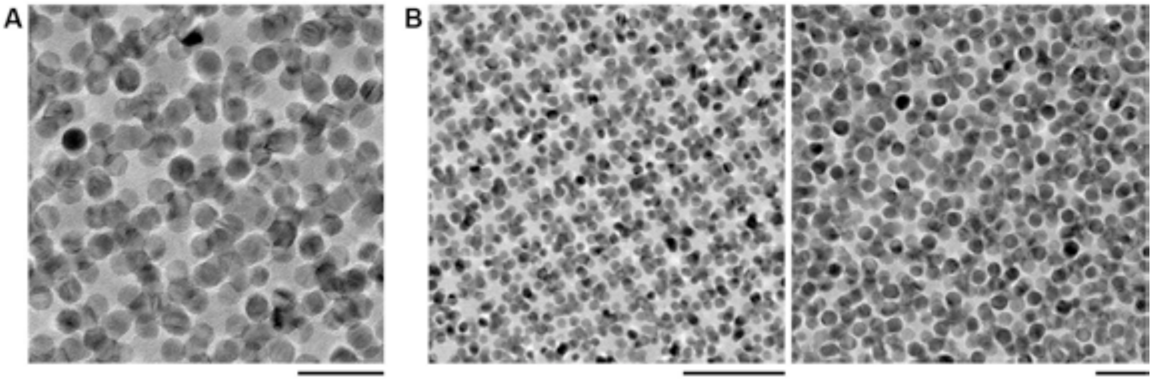

Fig. S23.

(**A**) TEM image of an AB_{11}-type BNSL containing NP septets in the top layer of Au NPs. (**B**) TEM images of the corresponding (post-etching) vac_1Au_{11}-type array. The scale bars correspond to 20 nm (A), 50 nm (B, *left*), and 20 nm (B, *right*).

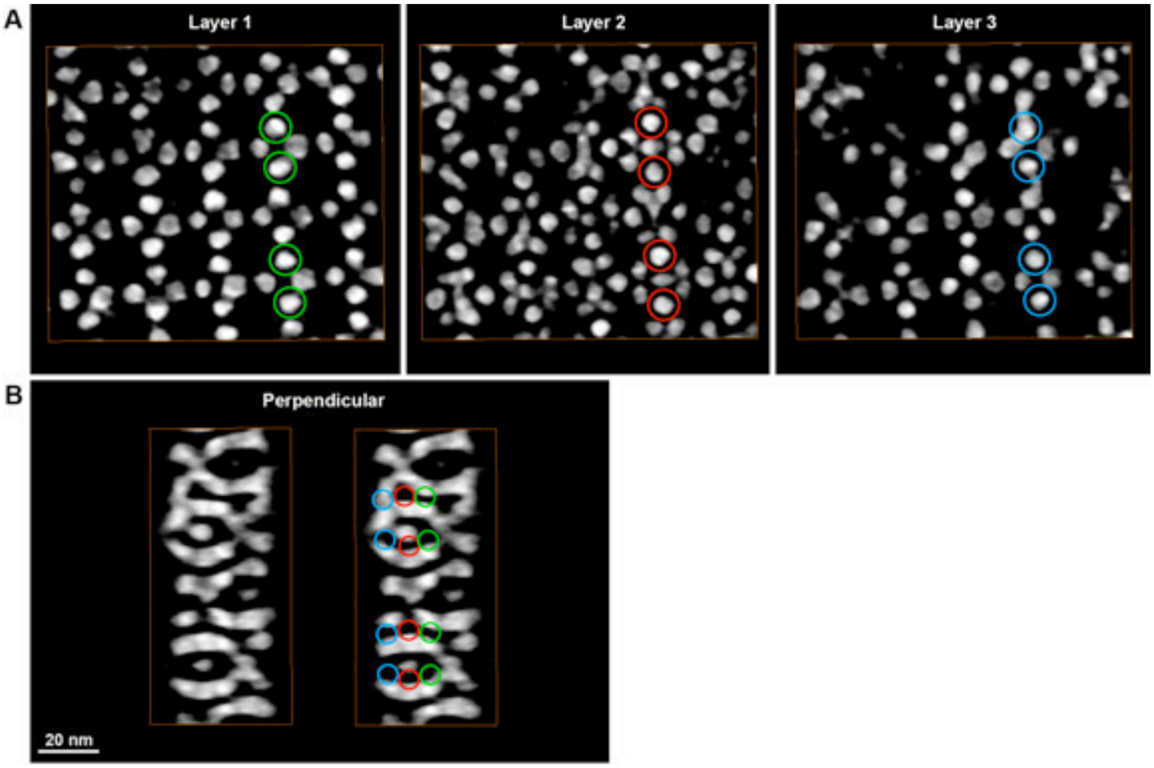

Fig. S24. Orthoslices through the reconstructed volume of the AB_{11} -type BNSL

(**A**) Orthoslices presenting the initial three layers of the structure. (**B**) Orthoslice through the reconstructed volume rotated 90° clockwise along the y-axis with respect to the orthoslices in the upper panel. The differently colored circles on the right correspond to the locations indicated in (A). As can be seen, a combination of missing wedge artifacts and sintering makes it difficult to resolve individual NPs along this direction. HAADF-STEM tomography series in our studies were acquired by using an aberration-corrected 'cubed' FEI-Titan electron microscope operated at 300 kV. Electron tomography series were acquired manually by using a Fischione model 2020 single-tilt tomography holder and reconstructed by using the simultaneous iterative reconstruction algorithm (SIRT) implemented in the ASTRA toolbox (*39*). For the SIRT reconstructions, 120 iterations were used.

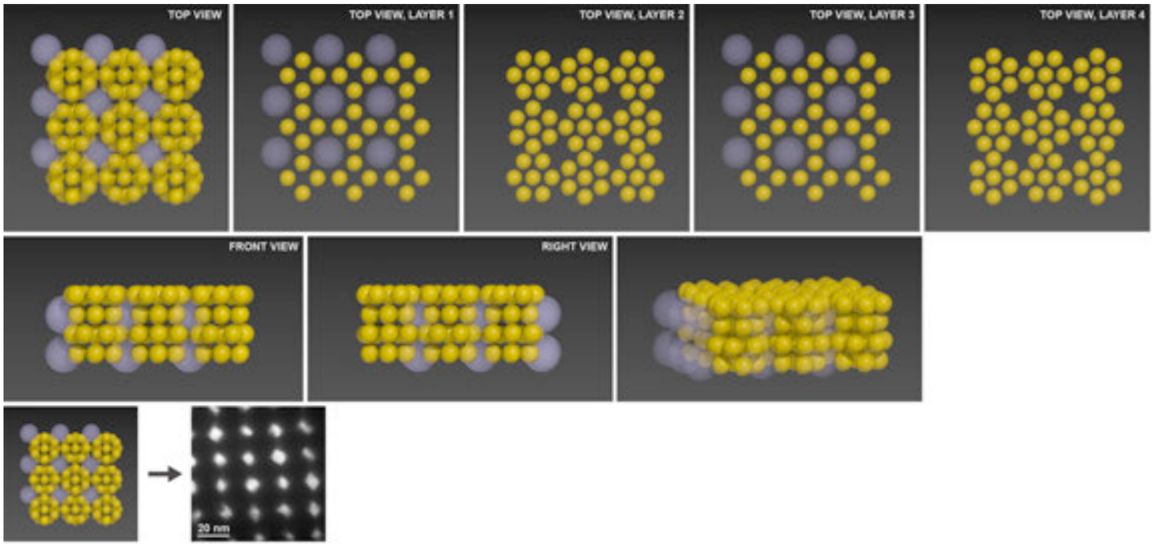

Fig. S25.

Structural model of the $\mathit{vac}_1\mathrm{Au}_{11}$-type array. *Bottom*: Prolonged thermal treatment of the precursor BNSL results in partial sintering of Au NPs, resulting in the formation of a nanoporous membrane featuring regular arrays of nanopores (here, 7.0 ± 0.8 nm).

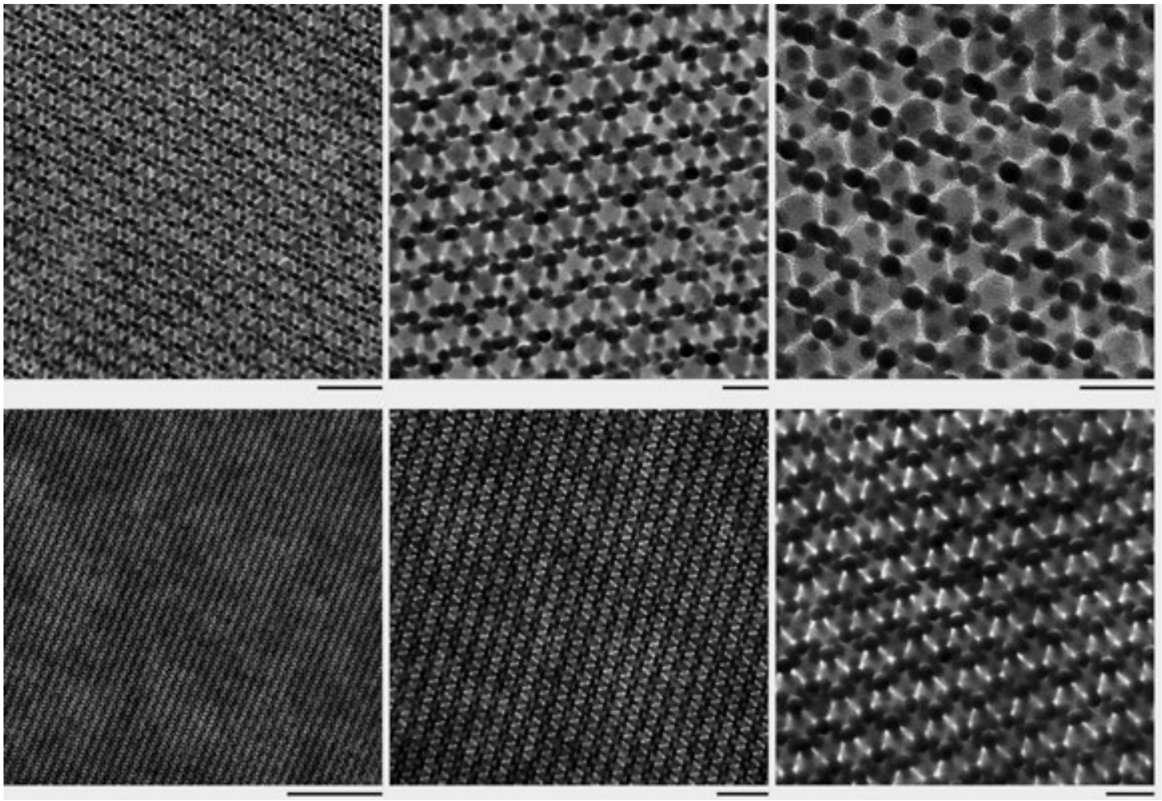

Fig. S26.

TEM images of AB_4-type BNSLs. The images in the top row correspond to monolayers of the AB_4 BNSL; the images in the bottom row are of thicker arrays. The scale bars correspond to (top row, L to R) 50 nm, 20 nm, and 20 nm, and (bottom row, L to R) 200 nm, 50 nm, and 20 nm.

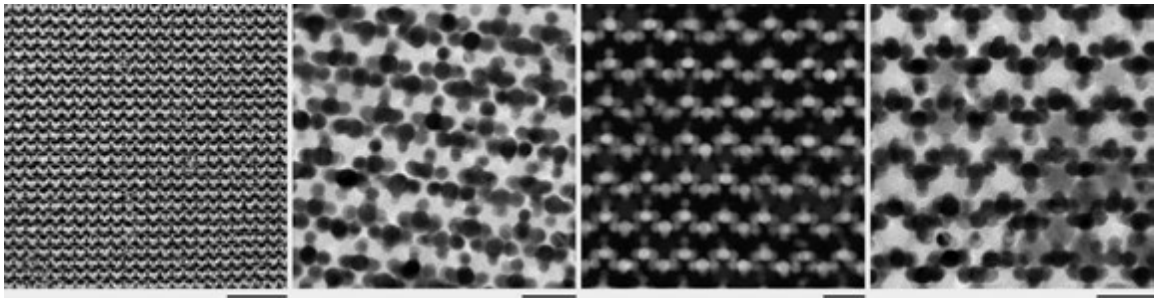

Fig. S27.

TEM and HAADF-STEM images of the $vac_1Au_1Au'_2Au''_1$-type array. The TEM image on the right was recorded before the complete etching of Fe_3O_4 NPs. The scale bars correspond to (L to R) 100 nm, 20 nm, 20 nm, and 20 nm.

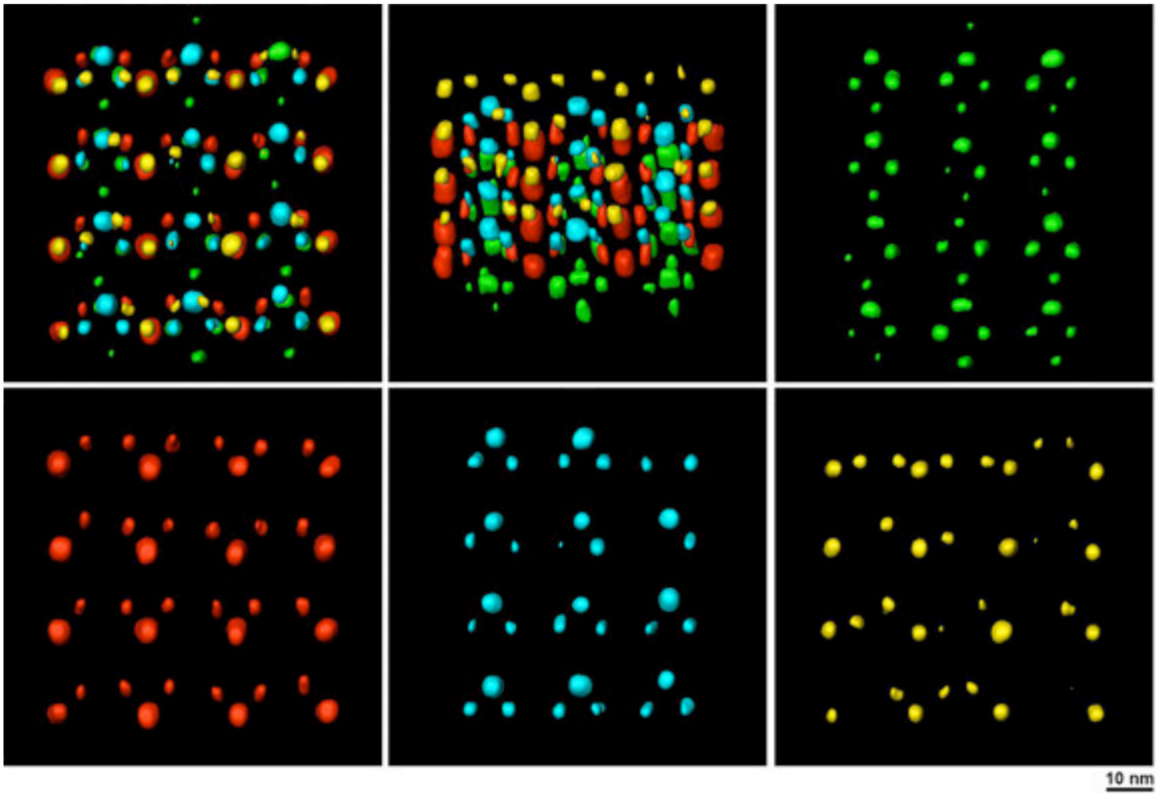

Fig. S28.

3D representations of a part of the reconstructed segmented volume of a *vac*$_1$Au$_1$Au$'_2$Au$''_1$-type array at different viewing directions. Note that the sample imaged here contained defects (some Au NPs are missing).

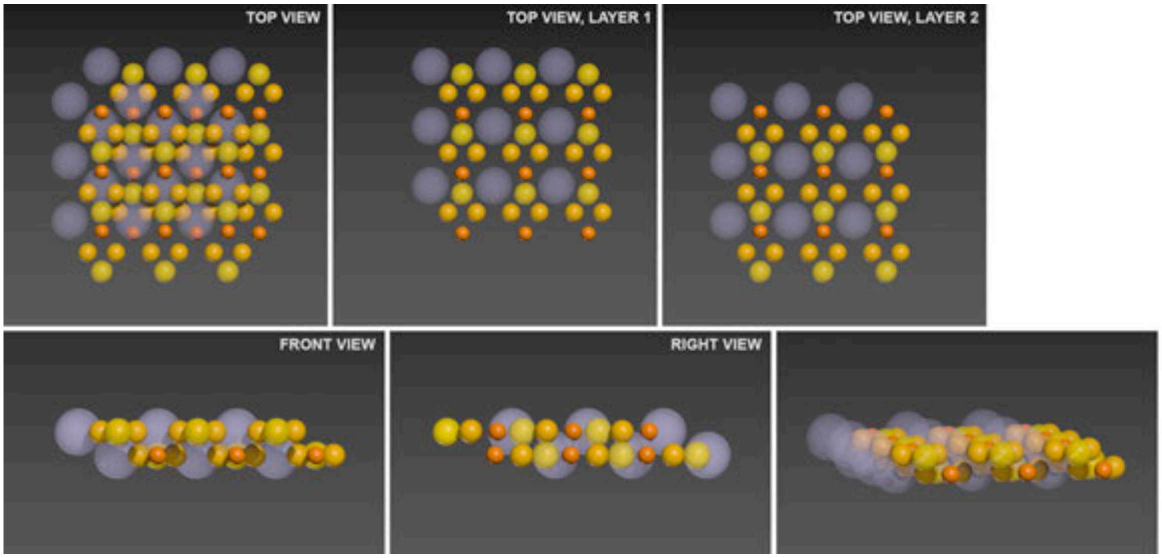

Fig. S29.

Structural model of the $\mathit{vac}_1\mathrm{Au}_1\mathrm{Au}'_2\mathrm{Au}''_1$-type array. Gold NPs of three different sizes are shown in light yellow, dark yellow, and orange.

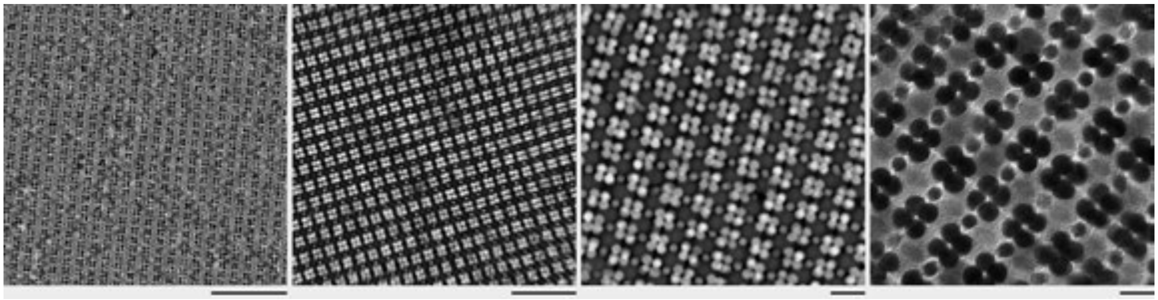

Fig. S30.

TEM and HAADF-STEM images of the ABC$_4$-type arrays. The scale bars correspond to (L to R) 100 nm, 50 nm, 20 nm, and 10 nm.

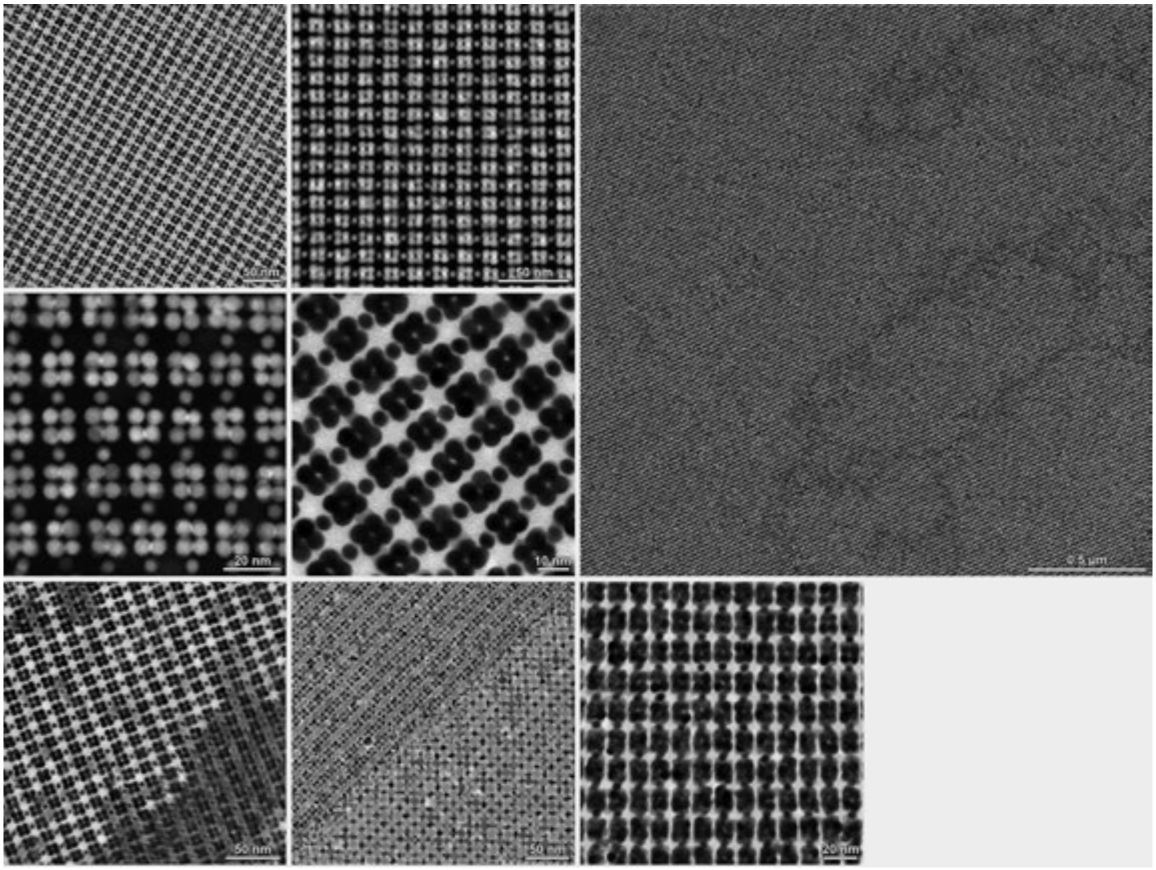

Fig. S31.

TEM and HAADF-STEM images of the $vac_1Au_4Au'_1$-type arrays. The TEM image in the bottom left was recorded before the complete etching of Fe_3O_4 NPs. The image next to it shows the coexistence of ABC_4- and AB_5-type BNSL. The expanded image in the top right shows an example of a large-scale, virtually defect-free array of $vac_1Au_4Au'_1$. The image in the bottom right shows a multilayer of the $vac_1Au_4Au'_1$-type array.

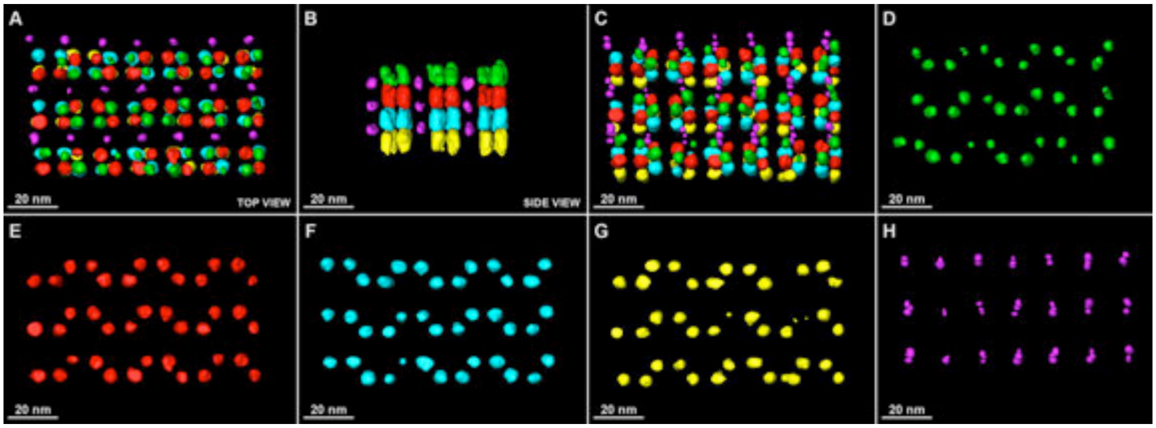

Fig. S32.

3D representations of a part of the reconstructed segmented volume of the $vac_1Au_1Au'_4$-type array at different viewing directions. In B, the volume is rotated 90° along the *y*-axis. In C, the structure is tilted by 8-10° along the *z*-axis. The images in D-G are views from the top; in H, the structure viewed from the top has been slightly rotated to highlight the presence of multiple layers. The different colors correspond to different segments along the *z*-axis.

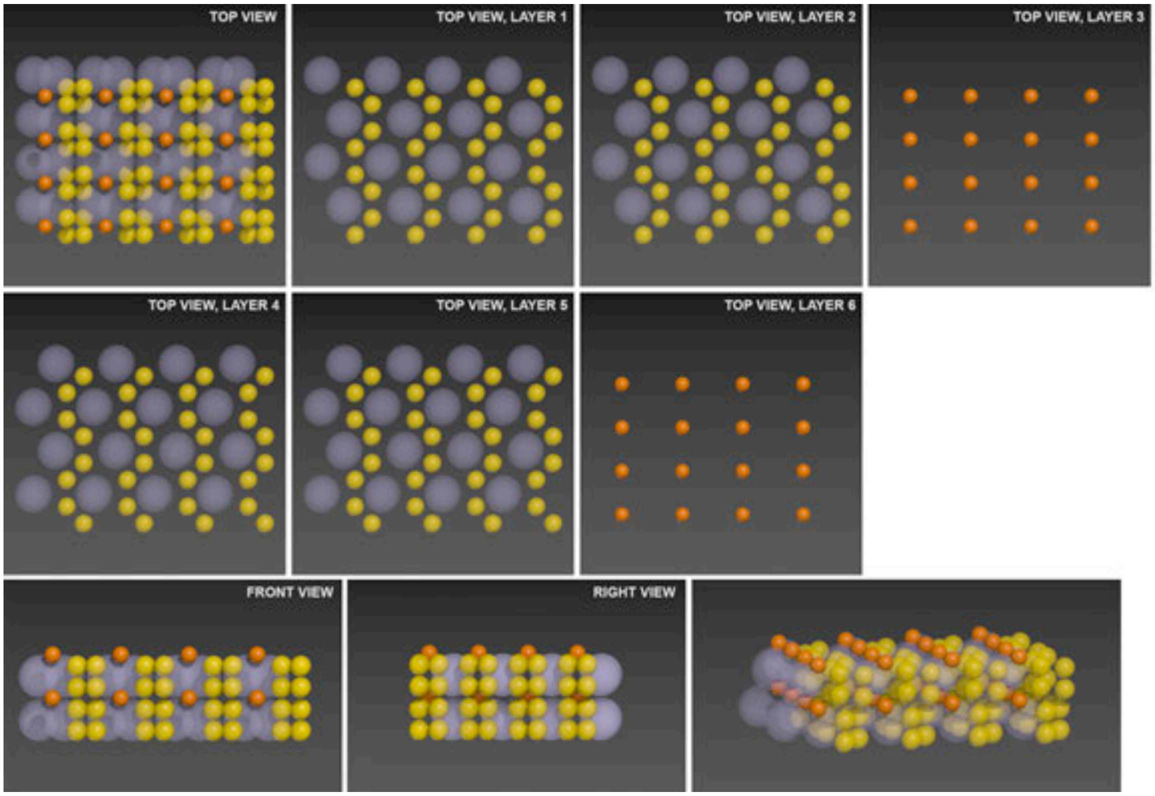

Fig. S33.

Structural model of the $\mathit{vac}_1\mathrm{Au}_4\mathrm{Au}'_1$-type array. Gold NPs of two different sizes are shown in yellow and orange.

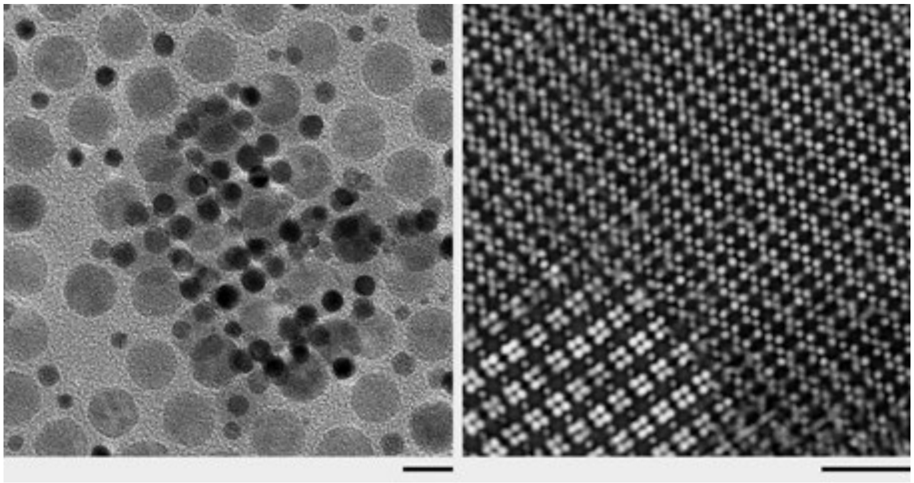

Fig. S34. Insights into the high stability of the ABC_4-type BNSL

Left: TEM image of a very small domain of the ABC_4-type BNSL. Notably, the domain is at least four Au NP-high (i.e., tetralayer), despite being surrounded by a sub-monolayer of NPs. *Right*: HAADF-STEM image showing a grain boundary between a $vac_1Au_1Au'_4$ and a vac_1Au_4 non-close-packed NP array (obtained by etching ABC_4-type and AB_4-type BNSLs, respectively) (note the epitaxial relationship) (in our experiments, we observed the coexistence of these two types of structures only once). The fact that the $vac_1Au_1Au'_4$ array in the bottom left of the HAADF-STEM image appears much brighter indicates that it is composed on a larger number of vertically stacked Au NPs. The scale bars correspond to 10 nm (L) and 50 nm (R).

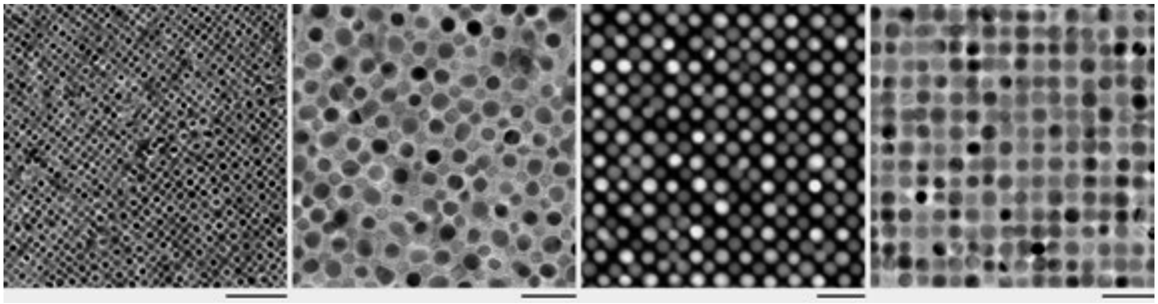

Fig. S35.

TEM and HAADF-STEM images of the “type I” bilayer of the *vac*$_1$Au$_1$-type array. The scale bars correspond to (L to R) 50 nm, 20 nm, 20 nm, and 20 nm.

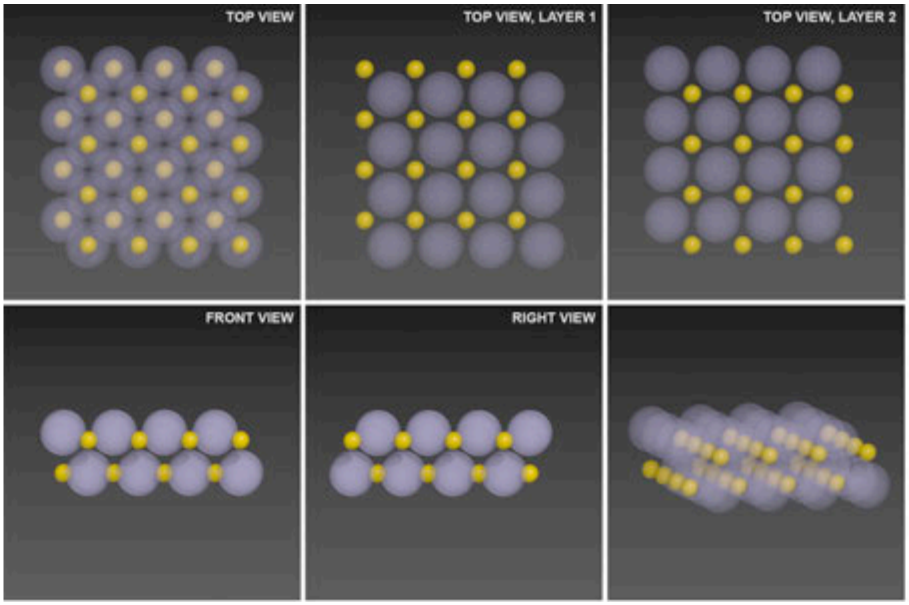

Fig. S36.
Structural model of the “type I” bilayer of the *vac*$_1$Au$_1$-type array.

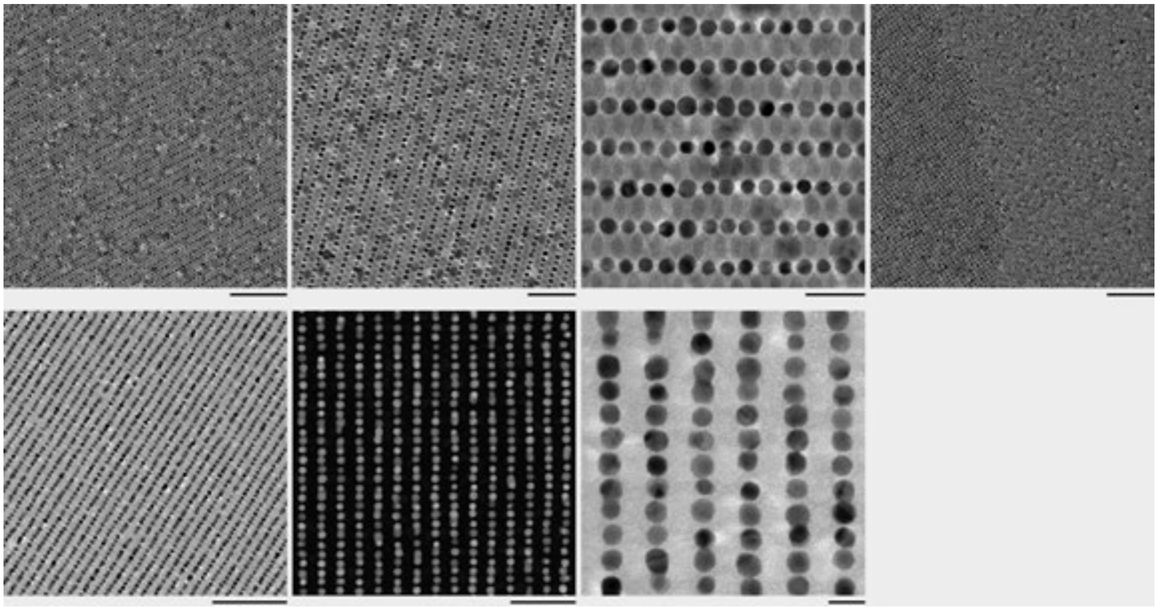

Fig. S37.

Top: TEM images of the “type II” bilayer of the AB-/NaCl-type BNSL. The scale bars correspond to (L to R) 100 nm, 50 nm, 20 nm, and 200 nm. *Bottom*: TEM and HAADF-STEM images of a bilayer of the *vac*$_1$Au$_1$-type array, where the two layers are stacked differently than in the samples shown in Fig. S35. The scale bars correspond to (L to R) 100 nm, 50 nm, and 10 nm.

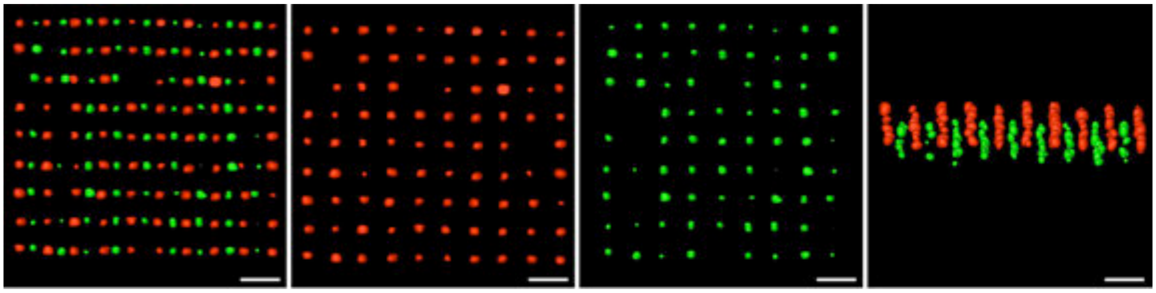

Fig. S38.

3D representations of a part of the reconstructed segmented volume of the “type II” bilayer of the *vac*$_1$Au$_1$-type array at different viewing directions. The scale bars correspond to 20 nm.

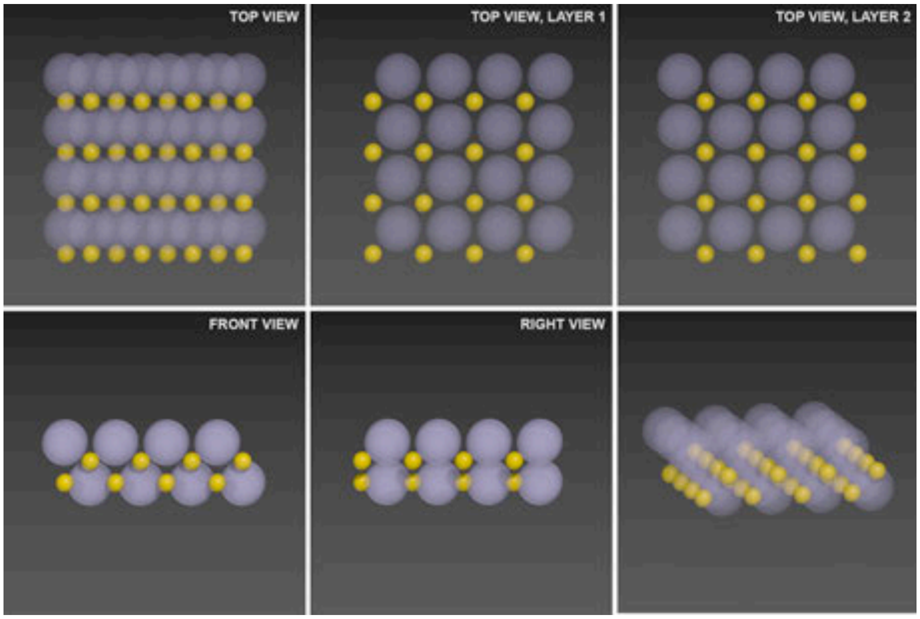

Fig. S39.
Structural model of the “type II” bilayer of the *vac*$_1$Au$_1$-type array.

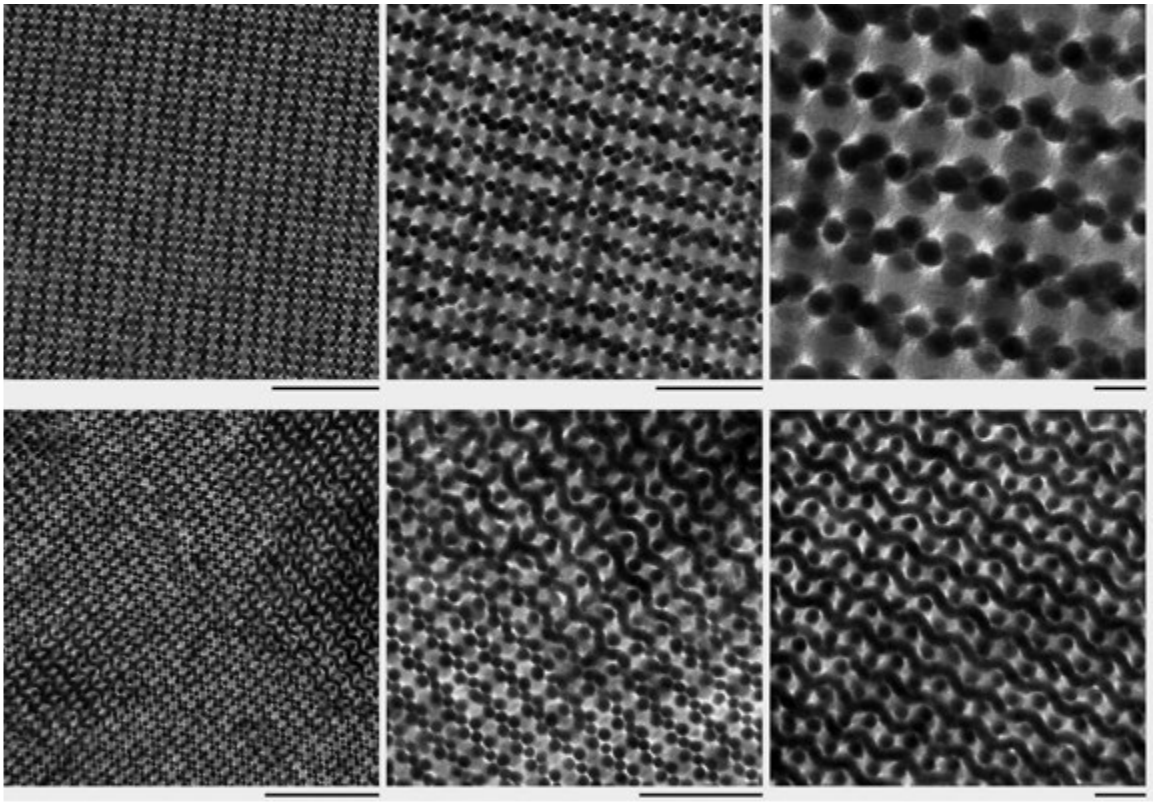

Fig. S40.

Top: TEM images of an AB_4-type BNSLs. The scale bars correspond to (L to R) 100 nm, 50 nm, and 10 nm. *Bottom*: TEM images of an AB_4-type BNSLs having undergone partial (center) or complete transformation into another type of AB_4-type BNSL. The scale bars correspond to (L to R) 100 nm, 50 nm, and 20 nm.

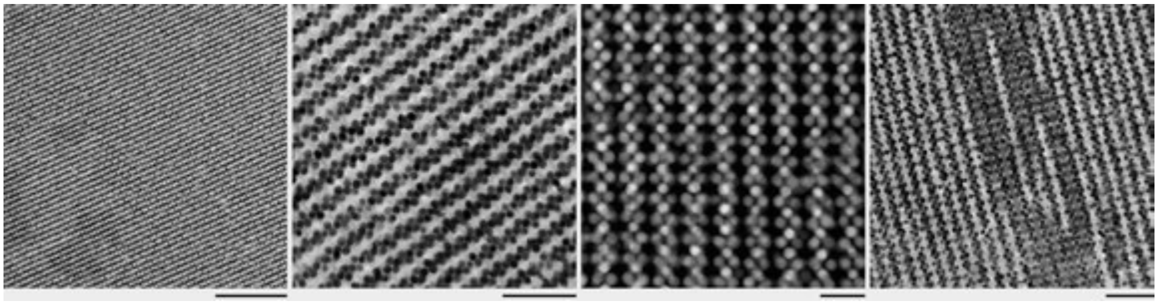

Fig. S41.

TEM and HAADF-STEM images of the *vac*$_1$Au$_4$-type array. Note that the image on the right was recorded before a complete etching of the Fe$_3$O$_4$ NPs. The scale bars correspond to (L to R) 200 nm, 50 nm, 20 nm, and 50 nm.

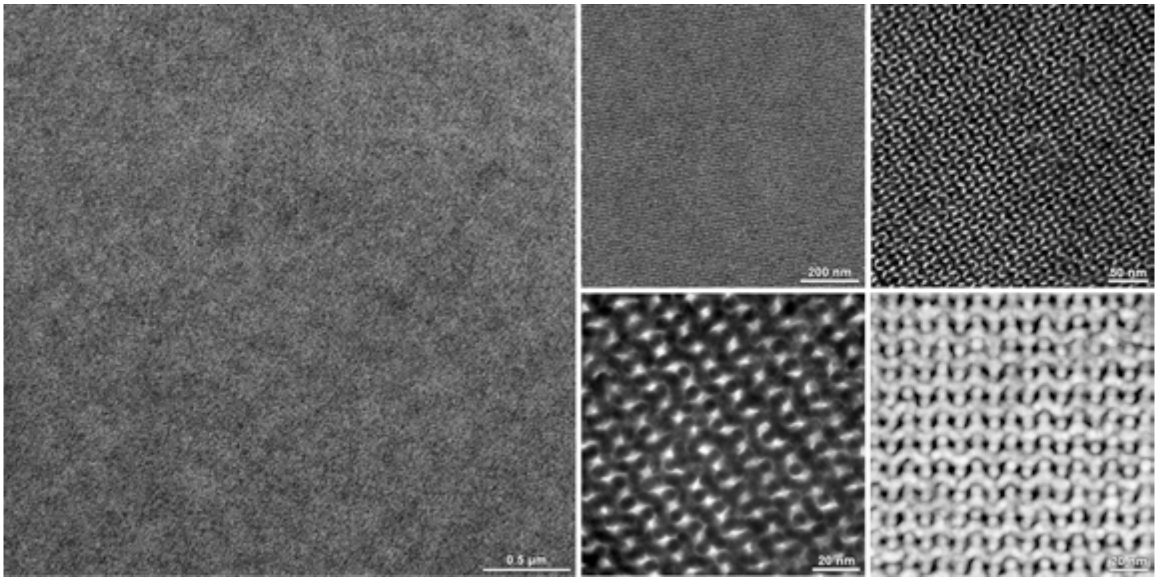

Fig. S42.
TEM and HAADF-STEM images of the *vac*$_1$Au$_4$-type array.

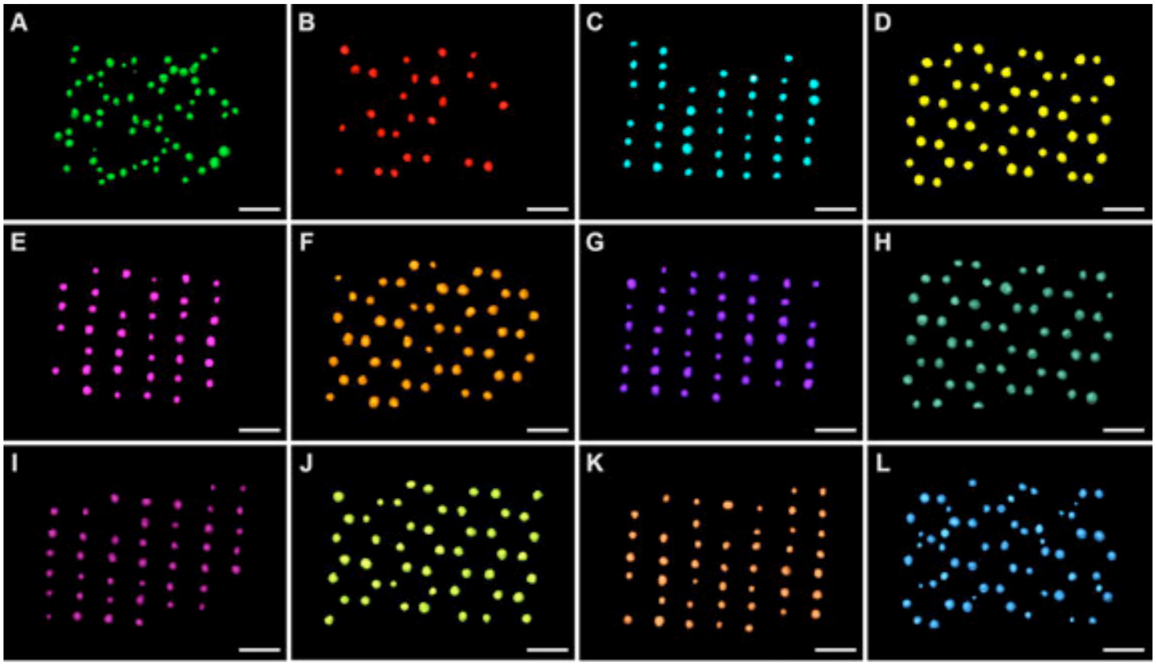

Fig. S43.

Different layers of the *vac*$_1$Au$_4$-type array shown in Fig. 3C. The scale bars correspond to 20 nm.

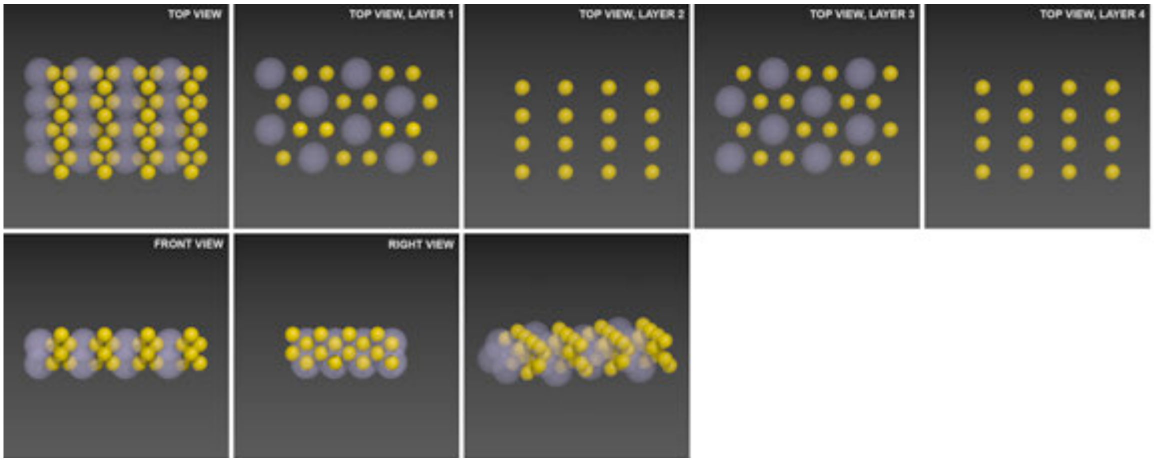

Fig. S44.

Structural model of the *vac*$_1$Au$_4$-type array.

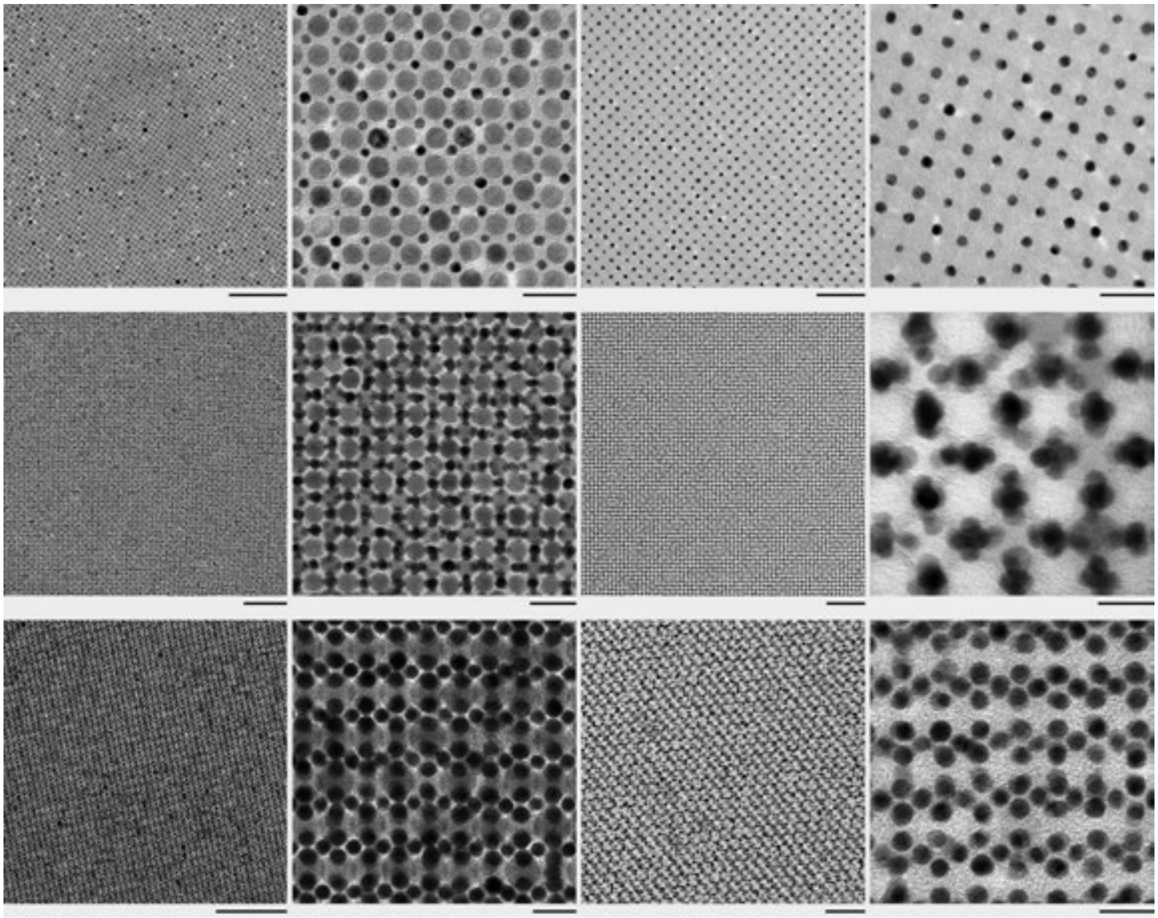

Fig. S45.

TEM images of binary superlattices co-assembled from 8.4 nm Fe_3O_4 NPs + 3.0 nm Au NPs and the resulting non-close-packed arrays. *Top row*: An AB-type BNSL and the corresponding *vac*$_1$Au$_1$-type array. The scale bars correspond to (L to R) 100 nm, 20 nm, 50 nm, and 20 nm. *Middle row*: An AB$_6$-type BNSL (without the top layer of Au NPs) and the corresponding *vac*$_1$Au$_5$-type array. The scale bars correspond to (L to R) 100 nm, 20 nm, 100 nm, and 10 nm. *Bottom row*: An AB$_4$-type BNSL and the corresponding *vac*$_1$Au$_4$-type array. The scale bars correspond to (L to R) 100 nm, 10 nm, 50 nm, and 10 nm.

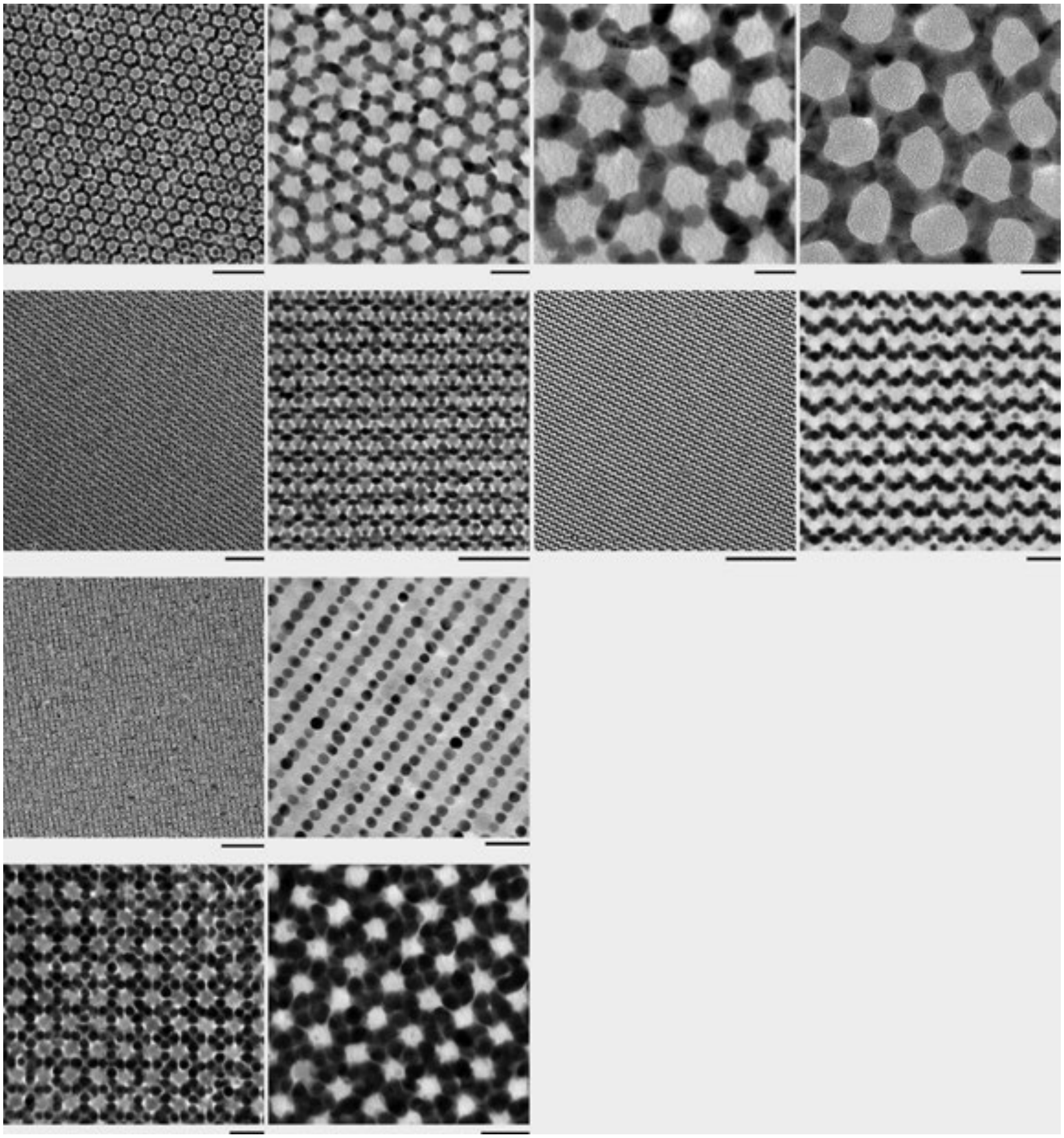

Fig. S46.

TEM images of binary superlattices co-assembled from 8.4 nm Fe_3O_4 NPs + 5.2 nm Au NPs and the resulting non-close-packed arrays. *First row* (L to R): An AB_5/$CaCu_5$-type BNSL; a vac_1Au_5-type array; a honeycomb membrane obtained by prolonged thermal treatment of the corresponding BNSL prior to etching; a honeycomb membrane obtained from a mixture of 10.6 nm Fe_3O_4 NPs and 5.2 nm Au NPs (taken from Fig. S14 for comparison). The scale bars correspond to (L to R) 50 nm, 20 nm, 10 nm, and 10 nm. *Second row*: An AB_4-type BNSL and the corresponding $vac_1Au_1Au_2'Au''_1$-type array. The scale bars correspond to 100 nm, 50 nm, 200 nm, and 20 nm. *Third row*: A bilayer of an AB-type BNSL and the corresponding vac_1Au_1-type array. The scale bars correspond to 100 nm (*left*) and 20 nm (*right*). Fourth row: An AB_{11}-type BNSL and the corresponding vac_1Au_{11}-type array. The scale bars correspond to 20 nm.

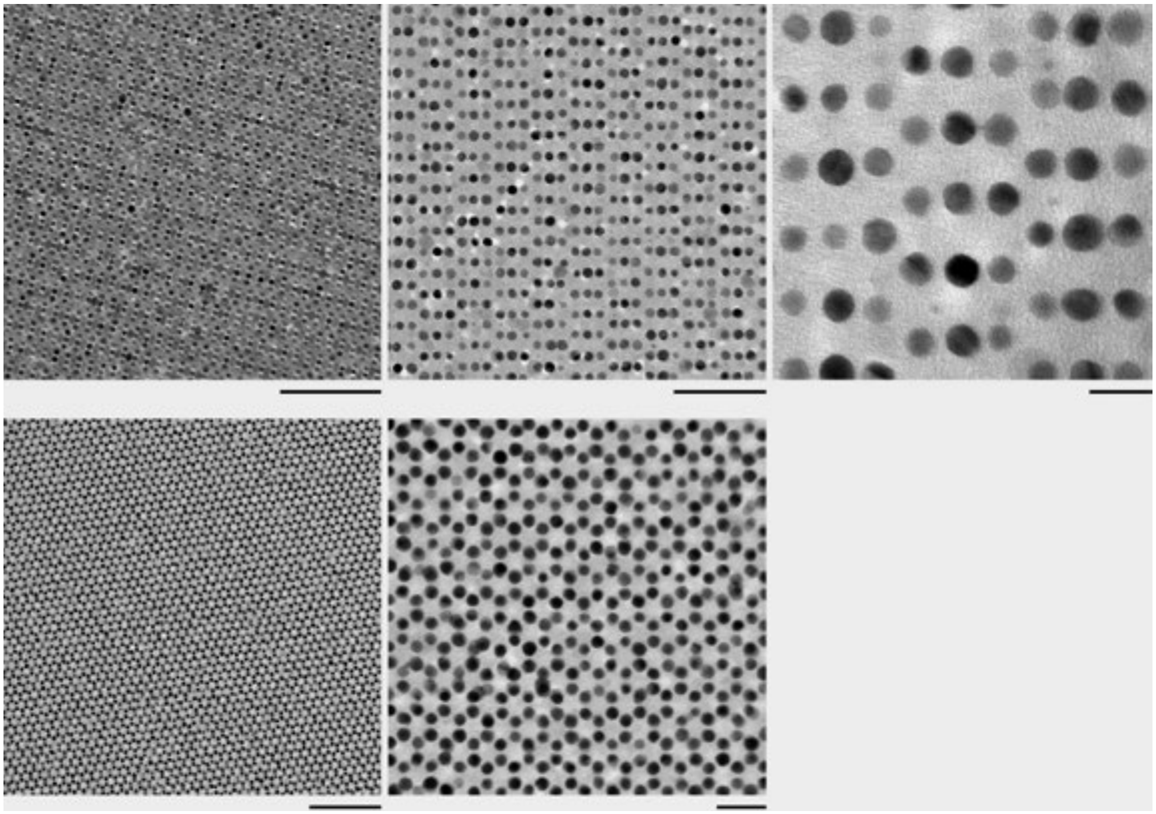

Fig. S47.

TEM images of additional binary superlattices obtained by co-assembly of 8.4 nm Fe_3O_4 NPs + 5.2 nm Au NPs and the resulting non-close-packed arrays. *Top*: An A_5B_3-type BNSL and the corresponding *vac*$_5$Au$_3$-type array. The scale bars correspond to (L to R) 100 nm, 50 nm, and 10 nm. *Bottom*: An AB_2-type BNSL and the corresponding *vac*$_1$Au$_2$-type array. The scale bars correspond to 100 nm (*left*) and 20 nm (*right*).

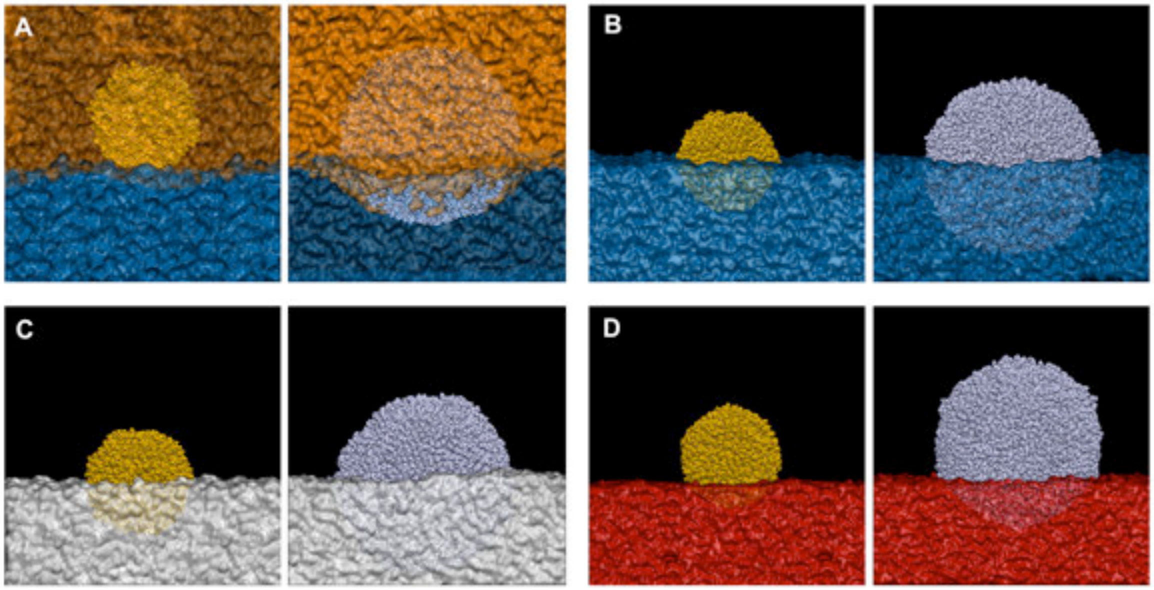

Fig. S48.

Individual Au NPs (on the left of each panel) and Fe_3O_4 NPs (on the right) relaxed at different interfaces: (**A**) DEG-hexane interface; (**B**) DEG-vacuum interface; (**C**) EG-vacuum interface; (**D**) water-vacuum interface. DEG, hexane, water, and EG are shown in dark blue, orange, dark, red, and light gray, respectively. Au NPs and Fe_3O_4 NPs are shown in yellow and light purple, respectively. Transparency levels of orange and blue surfaces in panel **A** are modulated for clarity so that Au NP is visible when immersed fully in hexane, and hexane is visible when Fe_3O_4 NP is almost fully immersed in hexane during the course of simulations.

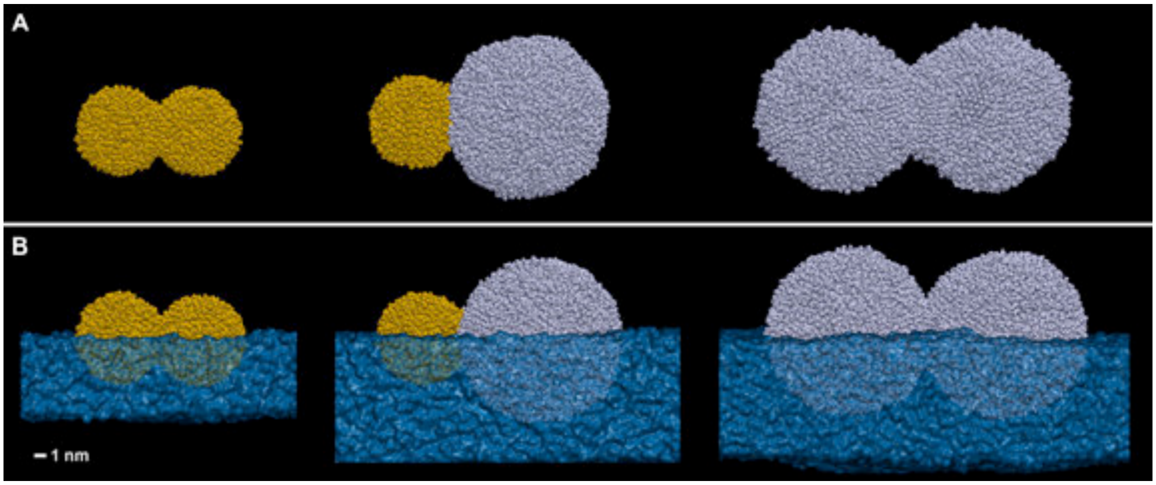

Fig. S49.

Nanoparticle pairs in vacuum (**A**) and at the DEG-vacuum interface (**B**) after 40 ns and 32 ns of simulations, respectively. From the left to the right: a pair of Au NPs; a pair of Au NP and Fe_3O_4 NP; a pair of Fe_3O_4 NPs. Au NPs are shown in yellow and Fe_3O_4 NPs in light purple. DEG is shown in dark blue.

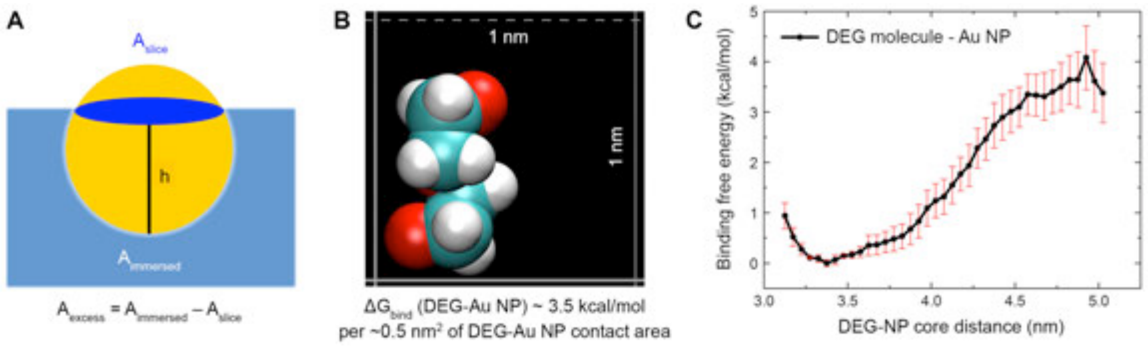

Fig. S50.

Estimating energy change upon immersing a dodacenethiol-functionalized Au NP from the DEG-vacuum interface into DEG. (**A**) Scheme of a partially immersed NP. Surface area of the immersed NP can be calculated as the surface area of the spherical cap without the base, $A_{immersed} = 2\pi Rh$, where R is the radius of the ligand-functionalized gold NP estimated as ~3.5 nm, and h is the immersion height defined in the scheme. The surface area of the slice shown (i.e., the surface area of the solvent prior to NP immersion) can be calculated as the area of the base of the spherical cap, $A_{slice} = \pi(2Rh–h^2)$. (**B**) The size of a single DEG molecule; the contact area between the DEG molecule and a gold NP surface is estimated as ~0.5 nm^2. (**C**) Free energy of binding between a single DEG molecule and a gold NP in vacuum, determined in umbrella sampling calculations. See also Fig. 2J in the main text.

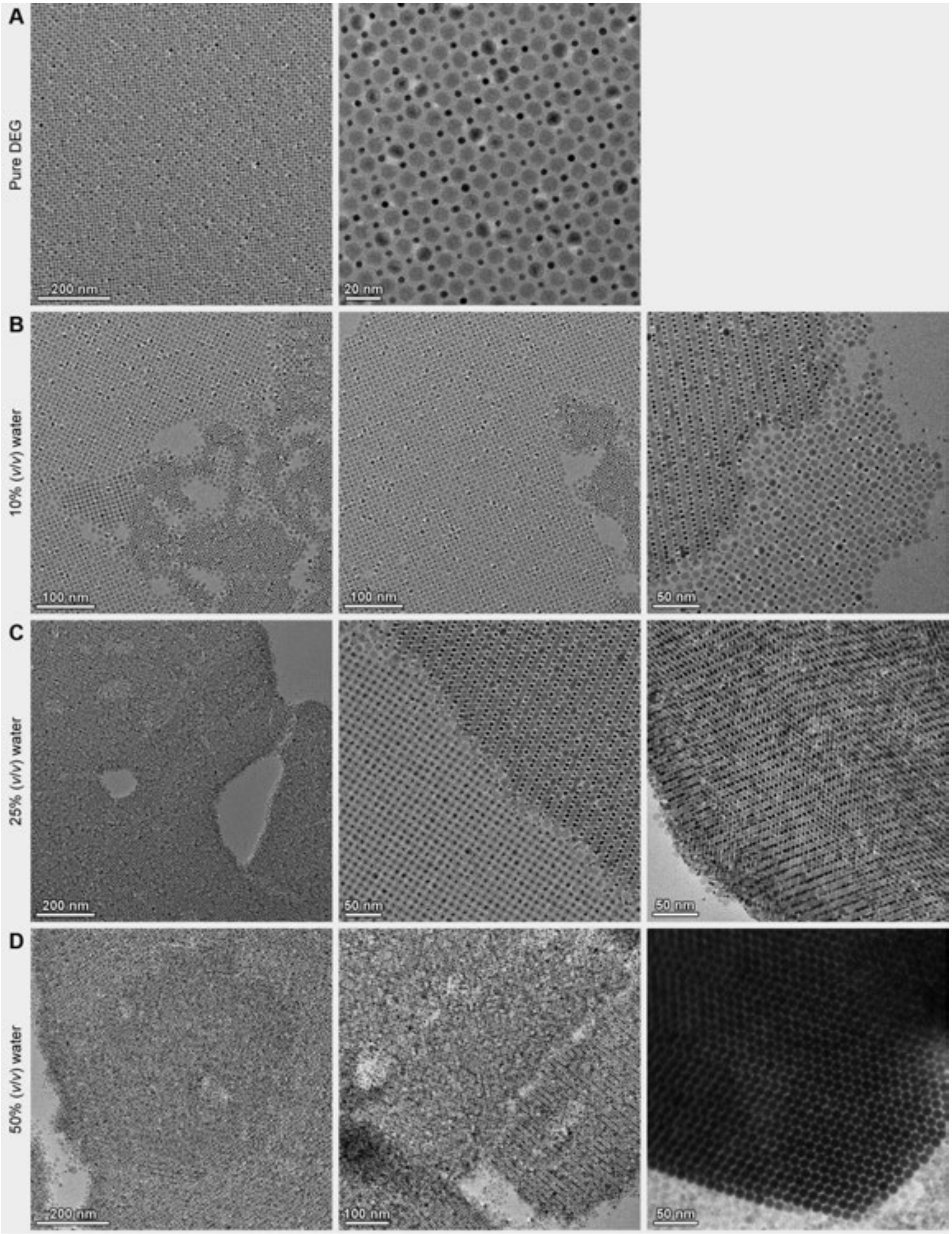

Fig. S51. Effect of the underlying liquid on Au-Fe_3O_4 BNSLs

Representative TEM images of NP superlattices obtained from the same 1:1 mixture of 5 nm Au NPs and 10 nm Fe_3O_4 NPs applied onto different liquids: (**A**) DEG, (**B**) 9:1 DEG-water, (**C**) 3:1 DEG-water, and (**D**) 1:1 DEG-water.

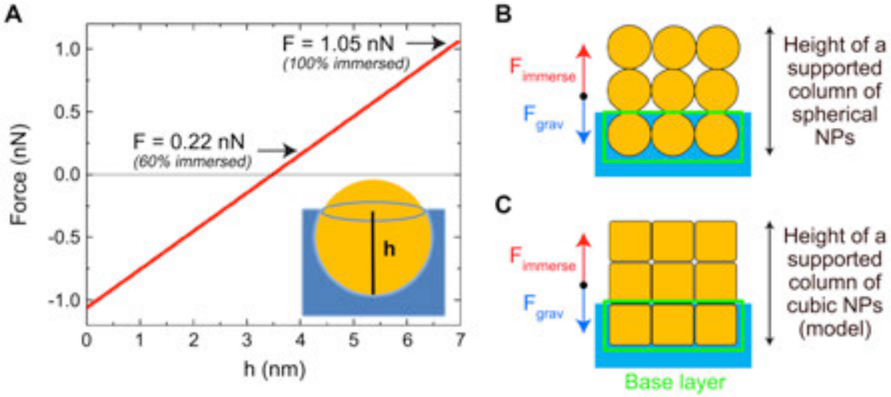

Fig. S52. Forces associated with the immersion of individual NPs and NP superlattices

(A) Net force acting on a dodecanethiol-functionalized spherical Au NP as a function of its immersion height in DEG. The NP has an effective diameter of 7 nm to account for the presence of dodecanethiol ligands on the gold core. The force is linearly dependent on height, giving a zero value for an approximately half-immersed NP (equilibrium) and a maximum value of 1.05 nN at 100% immersion. **(B)** Forces acting on a superlattice of self-assembled spherical NPs positioned at the DEG-vacuum interface (side view). Forces associated with the superlattice solvation ($F_{immerse}$) oppose immersion, while the gravitational force (F_{grav}) favors immersion. **(C)** The same analysis was used to examine a model superlattice formed by cubic NPs (see Table S5).

System	**Interaction energy** (kcal/mol)
Au NP / DEG	–1,200
Fe_3O_4 NP / DEG	–4,450
Au NP / EG	–1,300
Fe_3O_4 NP / EG	–5,400
Au NP / H_2O	–400
Fe_3O_4 NP / H_2O	–1,900

Table S1.

Interaction energies (enthalpies) between individual NPs and DEG, EG, and water equilibrated at liquid-vacuum interfaces.

NP system	**Interaction energy** (kcal/mol)
Au-Au in vacuum	–250
Au-Fe_3O_4 in vacuum	–320
Fe_3O_4-Fe_3O_4 in vacuum	–480
Au-Au at the DEG-vacuum interface	–200
Au-Fe_3O_4 at the DEG-vacuum interface	–205
Fe_3O_4-Fe_3O_4 at the DEG-vacuum interface	–440

Table S2.

Interaction energies between NPs in NP pairs simulated in vacuum and at the DEG-vacuum interface.

	NPs per unit cell		*Contact types and their counts*					
BNSL	**Au**	**Fe_3O_4**	**Au-DEG**	**Fe_3O_4-DEG**	**Au-Au**	**Au-Fe_3O_4**	**Fe_3O_4-Fe_3O_4**	**E** (kcal/mol)
AB_4	8	2	4	1	9	20	0	17,900
AB_6	12	2	4	1	12	24	0	19,930
AB_{11}	22	2	4	1	50	24	1	29,910

Table S3.

Lattice energies of selected experimentally observed BNSLs.

Number of 7 nm NPs in the base layer	**Force required to immerse the base layer** (N)	**Gravitational force on the base layer** (N)	**Number of layers supported***	**Number of 7 nm NPs supported***	**Height of the supported column** (m)
1 x 1	$2.18 \cdot 10^{-10}$	$2.16 \cdot 10^{-20}$	$1.01 \cdot 10^{10}$	$1.01 \cdot 10^{10}$	70.6
7 x 7	$1.07 \cdot 10^{-8}$	$1.06 \cdot 10^{-18}$	$1.01 \cdot 10^{10}$	$4.95 \cdot 10^{11}$	70.6
71 x 71	$1.10 \cdot 10^{-6}$	$1.09 \cdot 10^{-16}$	$1.01 \cdot 10^{10}$	$5.09 \cdot 10^{13}$	70.6

Table S4.

Solvation and gravitational forces acting on superlattices assembled from spherical NPs at the DEG-vacuum interface. (*) The estimated numbers in columns 4 and 5 are obtained by assuming that the force required to immerse the system is equal to the gravitational force. The calculation of the forces required to immerse the system utilizes the dodecanethiol-DEG free energy of binding of G° = –7 kcal/(mol nm^2). For simplicity, it is assumed that the NPs are immersed only by 60% of their height. The blue row highlights a superlattice comprising ~$5 \cdot 10^{11}$ NPs, which is estimated to be the total number of NPs in our experimental system (estimated from experiments in which 10 μL hexane droplets containing 0.1 mg/mL of NPs are deposited onto DEG).

Size of the system's base (nm^2)	Number of 7 nm NPs in the system's base	Force required to immerse the system (N)	Gravitational force on one "system NP" (N)	Number of "system NPs" supported	Number of 7 nm NPs supported*	Height of the supported column	Number of 7 nm NPs in the immersed lattice
1 x 1	1 x 1	$4.51 \cdot 10^{-10}$	$6.49 \cdot 10^{-20}$	$6.9416 \cdot 10^{9}$	$6.94 \cdot 10^{9}$	48.6 m	$6.94 \cdot 10^{9}$
50 x 50	7 x 7	$3.22 \cdot 10^{-9}$	$2.36 \cdot 10^{-17}$	$1.3605 \cdot 10^{8}$	$9.71 \cdot 10^{8}$	6.8 m	$4.8 \cdot 10^{10}$
500 x 500	71 x 71	$3.22 \cdot 10^{-8}$	$2.36 \cdot 10^{-14}$	$1.3605 \cdot 10^{6}$	$9.71 \cdot 10^{7}$	68 cm	$4.9 \cdot 10^{11}$
$5 \cdot 10^3$ x $5 \cdot 10^3$	714 x 714	$3.22 \cdot 10^{-7}$	$2.36 \cdot 10^{-11}$	$1.3605 \cdot 10^{4}$	$9.71 \cdot 10^{6}$	6.8 cm	$4.9 \cdot 10^{12}$
$5 \cdot 10^4$ x $5 \cdot 10^4$	7,140 x 7,140	$3.22 \cdot 10^{-6}$	$2.36 \cdot 10^{-8}$	$1.3605 \cdot 10^{2}$	$9.71 \cdot 10^{5}$	6.8 mm	$4.9 \cdot 10^{13}$
$5 \cdot 10^5$ x $5 \cdot 10^5$	71,400 x 71,400	$3.22 \cdot 10^{-5}$	$2.36 \cdot 10^{-5}$	$1.3605 \cdot 10^{0}$	$9.71 \cdot 10^{4}$	0.68 mm	$4.9 \cdot 10^{14}$

Table S5.

Solvation and gravitational forces acting on superlattices assembled from cubic NPs at the DEG-vacuum interface. (*) The estimated numbers in columns 5 and 6 were obtained assuming that the force required to immerse the system is equal to the gravitational force. The calculation of the solvation forces uses a scaled-down dodecanethiol-DEG free energy of binding, where G° ~ –4.7 kcal/(mol nm^2). The blue row highlights the superlattice comprising ~$5 \cdot 10^{11}$ NPs, which is estimated to be the total number of NPs in our typical experimental system.

Database S1.

The database includes electron tomography data and is publicly accessible under the links provided below.

- *vac*$_1$Au$_5$-type array:
  http://ematweb.uantwerpen.be/colouratoms/jsc3D/demos/vac1Au5.html
- *vac*$_1$Au$_{11}$-type array:
  http://ematweb.uantwerpen.be/colouratoms/jsc3D/demos/vac1Au11.html
- *vac*$_1$Au$_1$Au$_2{}'$Au$''_1$-type array:
  http://ematweb.uantwerpen.be/colouratoms/jsc3D/demos/vac1Au1Au2Au1.html
- *vac*$_1$Au$_1$Au$'_4$-type array:
  http://ematweb.uantwerpen.be/colouratoms/jsc3D/demos/vac1Au1Au4.html
- *vac*$_1$Au$_4$-type array:
  http://ematweb.uantwerpen.be/colouratoms/jsc3D/demos/vac1Au4.html
- *vac*$_1$Au$_1$-type array:
  http://ematweb.uantwerpen.be/colouratoms/jsc3D/demos/vac1Au1.html